Opto-Acoustic Image Reconstruction and Motion Tracking Using Convex Optimization

Jason Zalev and Michael C. Kolios, *Member, IEEE*

***Abstract*—Opto-acoustic imaging systems detect acoustic waves produced by optical absorption to visualize molecular contrast in biological tissue. This permits non-invasive vascular assessment of benign and malignant tumors. In this article, we describe a framework to iteratively determine the motion of an opto-acoustic probe during a minimization-based image reconstruction process. The probe emits light and uses an ultrasonic transducer array to acquire data for cross-sectional slices of tissue. To improve visibility, our technique uses multiple 2D slices to perform 3D volumetric reconstruction. Our model includes wavelength-specific optical absorption, position-dependent illumination and a realistic transducer element geometry. We investigate this technique using simulated, experimentally collected, and clinically acquired data. By performing 3D image reconstruction on a digital phantom, we demonstrate estimation of elevational probe motion without external sensors. We compare images of a benign lesion from a clinical breast imaging study and observe significant artifact reduction and contrast-to-background ratio improvement using our technique. The approach has potential to improve opto-acoustic image visibility for assessment of breast cancer or other diseases.**

***Index Terms*—Convex optimization, linear array trajectory, motion estimation, multi-wavelength 3D imaging, opto-acoustic image reconstruction.**

I. Introduction

RECENT clinical studies have investigated opto-acoustic imaging (OA) for assessment and diagnosis of breast cancer [1]–[11]. OA helps to visualize cancerous lesions, which are metabolically more active, and tend to have higher vascularity, irregular blood vessels, and decreased oxygen saturation compared to benign lesions and healthy tissue [12]–[16]. By using optical absorption to generate acoustic waves, the technology permits imaging of blood vessels and oxygenation levels in tumors located several centimeters beneath the skin, without using harmful ionizing radiation or injected contrast agents [4].

OA reconstruction involves generating images to visualize the molecular composition of tissue. To achieve this, acoustic transducer measurements are digitally processed to localize acoustic sources based on propagation delays. The use of multiple optical wavelengths allows molecular constituents to be determined from their optical absorption spectra. For proper tissue visualization, reconstructed images must have minimal clutter and distortion. Although several analytic inversion formulas exist for performing OA reconstruction [17]–[21], these generally cause distortion unless a reconstructed region of tissue is fully surrounded by detectors to capture all emitted acoustic waves. Consequently, the effectiveness of analytic reconstruction approaches is limited by tissue surface acquisition because complete acoustic capturing is not possible. To permit more accurate image reconstruction, convex mathematical optimization uses assumptions about spatial smoothness and image sparsity to fit reconstructed images onto measured data [22], [23], [23]–[27]. This can significantly improve contrast and reduce clutter. However, certain unwanted artifacts remain difficult to suppress, especially in 2D systems.

In 2D OA imaging, subjects are scanned using a hand-held probe that incorporates an ultrasonic linear-array transducer with an integrated light delivery unit [1]–[11]. The light distribution, which depends on the illumination geometry and optical wavelength, cannot easily be confined to a 2D slice of tissue. This results in interfering acoustic waves produced by out-of-plane optical absorbers. Moreover, light intensity attenuates exponentially, which limits optical penetration and decreases image contrast in deep tissue. Obtaining additional surface measurements can potentially overcome these limitations by improving image contrast, interference suppression, and acoustic source localization. However, with free-hand acquired data, this requires the linear array's position and orientation to be known and included in the reconstruction model. Consequently, there is a need for approaches that efficiently incorporate a probe's trajectory into 3D OA reconstruction.

In this article, we propose a method to reduce artifact and reconstruct 3D images, which simultaneously solves motion of an OA probe. This enables volumetric reconstruction from multiple 2D slices, which helps suppress interference and improve contrast in 2D imaging. The approach uses sequential convex optimization, and is based on fitting measured acoustic data onto a model's predicted response. We propose a novel model where a wavelength-specific light distribution is delivered from the probe's coordinate frame, and predicted acoustic signals are simulated based on 3D molecular composition of tissue. Fast computation is developed using a separable acoustic response matrix, described in our earlier work [28], which includes the array's position and orientation. We demonstrate reconstruction of 2D and 3D images with improved image quality compared to a formula-based approach.

Manuscript received February 16, 2021; revised June 30, 2021; accepted July 28, 2021. Date of publication September 14, 2021; date of current version November 9, 2021. This work was supported by the Natural Sciences and Engineering Research Council of Canada (NSERC) under Grant RGPIN-2017-06496. The associate editor coordinating the review of this manuscript and approving it for publication was Dr. Petros T. Boufounos. *(Corresponding author: Jason Zalev.)*

The authors are with the Department of Physics, Ryerson University, Toronto, ON M5G 1Z3, Canada (e-mail: jzalev@ryerson.ca; mkolios@ryerson.ca).

This article has supplementary downloadable material available at https://doi.org/10.1109/TCI.2021.3110742, provided by the authors.

Digital Object Identifier 10.1109/TCI.2021.3110742

To our best knowledge, this is the first work involving OA, where reconstruction and probe motion are simultaneously solved through a combined minimization objective. In the literature, numerous OA reconstruction approaches have been studied [17]–[20], [20]–[27], including formula-based back-projection [17]–[20] and mathematical optimization [22], [23], [23]–[27]. However, these involve different processing and assumptions compared to our approach. In OA, combined reconstruction methods have previously been considered to estimate non-rigid deformation with internal tissue motion [29], [30], but this is different from solving probe motion and requires many additional variables. In other work, sensors have been used to determine OA probe motion [31]. In ultrasound, motion tracking has been well studied [32]–[40], but previous sensor-free approaches involving ultrasonic speckle correlation are not fully applicable to OA. Moreover, out-of-plane artifact in 2D slices can interfere with correlation-based OA tracking. To overcome such limitations, one study correlated 3D volumes obtained with a matrix-array probe [41]. Our approach, which advantageously is applicable even in the presence of interference specific to 2D OA imaging, was inspired by combined alignment and reconstruction used in other modalities [42] and in computer vision [43]–[45].

This article is organized as follows. Section II-A provides theoretical background for opto-acoustic signal generation. Section II-B describes image reconstruction based on convex mathematical optimization. In Section III, we develop a system model, which simulates opto-acoustic signals for multiple 2D slices. Using this model, in Section IV we develop an algorithm for 3D image reconstruction and motion tracking. Section V describes the results and implementation. Additional results are provided as Supplemental Materials. Discussion is provided in Section VI. We conclude in Section VII. Table I lists symbols used throughout this work.

II. Background

A. Opto-Acoustic Signals

In opto-acoustic imaging, a probe delivers a rapid pulse of light, at *optical wavelength* λ, to the tissue surface. The *radiant fluence* $\varphi(\lambda, \mathbf{r})$ is the amount of light that reaches position $\mathbf{r}$ within the tissue. When light is absorbed, it is converted to an acoustic source distribution called the *initial excess pressure* $\psi(\lambda, \mathbf{r})$, which subsequently propagates as acoustic waves. This is equal to

$$\psi(\lambda, \mathbf{r}) = \eta(\lambda, \mathbf{r})\, \varphi(\lambda, \mathbf{r}), \tag{1}$$

where $\eta(\lambda, \mathbf{r})$ is the *opto-acoustic conversion efficiency*, which is given by

$$\eta(\lambda, \mathbf{r}) = \gamma(\mathbf{r})\, \mu_{\mathrm{a}}(\lambda, \mathbf{r}). \tag{2}$$

Here, $\eta(\lambda, \mathbf{r})$ is the product of the tissue *optical absorption coefficient* $\mu_{\mathrm{a}}(\lambda, \mathbf{r})$, which describes conversion of light to heat; and, the *Grüneisen parameter* $\gamma(\mathbf{r})$, which relates added heat to excess pressure. In tissue, γ typically has a small spatial variation, and is often assumed to be constant. The parameter μ_{a} depends on the abundance of light-absorbing molecules called *chromophores*, which are spatially distributed based on the tissue composition, and can have widely different wavelength-specific

TABLE I
List of Symbols

Symbol	Description
$\mathbf{y}_j \in \mathbb{R}^{n_{\mathrm{m}}}$	measured data for j-th frame $\mathbf{y} = \mathrm{vec}([\mathbf{y}_1, \mathbf{y}_2, \ldots, \mathbf{y}_{n_{\mathrm{f}}}])$
$\mathbf{x}_i \in \mathbb{R}^{n_{\mathrm{v}}}$	volume fraction abundance of i-th chromophore $X = [\mathbf{x}_1, \mathbf{x}_2, \ldots, \mathbf{x}_{n_\mu}] \in \mathbb{R}^{n_{\mathrm{v}} \times n_\mu}$ $\mathbf{x} = \mathrm{vec}(X) \in \mathbb{R}^{(n_{\mathrm{v}} n_\mu)}$
$H \in \mathbb{R}^{(n_{\mathrm{m}} n_{\mathrm{f}}) \times (n_{\mathrm{v}} n_\mu)}$	overall system matrix $H = \begin{bmatrix} H_1 \\ \vdots \\ H_{n_{\mathrm{f}}} \end{bmatrix}$
$H_j \in \mathbb{R}^{(n_{\mathrm{m}}) \times (n_{\mathrm{v}} n_\mu)}$	system matrix for j-th frame $H_j = H_0\, \Phi_{\lambda_j}\, T_{\mathbf{p}_j}\, M_{\lambda_j}$
$H_0 \in \mathbb{R}^{n_{\mathrm{m}} \times n_{\mathrm{v}}}$	acoustic response matrix $H_0 = F_0\, G_0$
$M_{\lambda_j} \in \mathbb{R}^{(n_{\mathrm{v}}) \times (n_{\mathrm{v}} n_\mu)}$	absorption matrix for wavelength λ_j $M_{\lambda_j} = \mathbf{m}_{\lambda_j} \otimes I_{n_{\mathrm{v}}}$
$\Phi_{\lambda_j} \in \mathbb{R}^{n_{\mathrm{v}} \times n_{\mathrm{v}}}$	optical illumination matrix for wavelength λ_j $\Phi_{\lambda_j} = \mathrm{diag}(\boldsymbol{\varphi}_{\lambda_j})$
$T_{\mathbf{p}_j} \in \mathbb{R}^{n_{\mathrm{v}} \times n_{\mathrm{v}}}$	transformation matrix for configuration $\mathbf{p}_j$
$\mathbf{p}_j \in \mathbb{R}^{n_{\mathrm{p}}}$	configuration parameters for j-th frame $\mathbf{p} = \mathrm{vec}([\mathbf{p}_1, \mathbf{p}_2, \ldots, \mathbf{p}_{n_{\mathrm{f}}}])$
$\Delta\mathbf{p}_j \in \mathbb{R}^{n_{\mathrm{p}}}$	change in configuration for j-th frame $\Delta\mathbf{p} = \mathrm{vec}([\Delta\mathbf{p}_1, \Delta\mathbf{p}_2, \ldots, \Delta\mathbf{p}_{n_{\mathrm{f}}}])$
$J_{\mathbf{p}_j} \in \mathbb{R}^{n_{\mathrm{m}} \times n_{\mathrm{p}}}$	Jacobian matrix for configuration $\mathbf{p}_j$
$A_j \in R^{3 \times 3}$	rotation matrix for j-th frame
$\mathbf{b}_j \in \mathbb{R}^3$	translation vector for j-th frame
$\boldsymbol{\theta}_j \in \mathbb{R}^3$	Euler angles for j-th frame (roll, pitch, yaw) $\mathbf{p}_j = \mathrm{vec}([\mathbf{b}_j, \boldsymbol{\theta}_j])$
$\vartheta \colon \mathbb{R}^{n_{\mathrm{v}} \times n_\mu} \to \mathbb{R}$	regularization function
$F_0 \in \mathbb{R}^{n_{\mathrm{m}} \times n_{\mathrm{m}'}}$	separable factor for in-plane slice
$G_0 \in \mathbb{R}^{n_{\mathrm{m}'} \times n_{\mathrm{v}}}$	separable factor for perpendicular slices
$\psi(\lambda, \mathbf{r})$	initial excess acoustic pressure
$\eta(\lambda, \mathbf{r})$	opto-acoustic conversion efficiency
$\varphi(\lambda, \mathbf{r})$	radiant fluence
$\mu_{\mathrm{a}}(\lambda, \mathbf{r})$	tissue optical absorption coefficient
$m_i(\lambda)$	optical absorption coefficient of chromophore i
$\chi_i(\mathbf{r})$	volume fraction abundance of chromophore i
$\gamma(\mathbf{r})$	Grüneisen parameter
$y(\lambda, \mathbf{r}, t)$	opto-acoustic signal amplitude
$h(\mathbf{r}, t)$	statio-temporal impulse response
$g'(\mathbf{r}, t)$	ideal impulse response
$f_{\mathbf{a}}(\mathbf{r})$	transducer aperture function
$\alpha(\mathbf{r})$	obliquity factor
$\beta(t)$	electro-mechanical impulse response
$\delta(t)$	Dirac delta function
c_0	speed of sound
t	elapsed time
$\mathbf{r} \in \mathbb{R}^3$	spatial position
λ	optical wavelength
λ_j	index for optical wavelength of j-th frame
$\mathbf{m}_{\lambda_j} \in \mathbb{R}^{n_\mu}$	optical absorption vector at wavelength λ_j
$y_j(\mathbf{r}_l, t)$	time-domain signal of transducer l in frame j
$\psi_j(\mathbf{r})$	initial excess pressure of frame j
$\tau_j(\mathbf{r})$	affine transform function for frame j
I_n	identity matrix of size n
$\otimes$	tensor product
$\odot$	Hadamard product (elementwise multiplication)
$n_{\mathrm{v}} = n_{\mathrm{x}} n_{\mathrm{y}} n_{\mathrm{z}}$	number of voxels (total and along xyz axes)
$n_{\mathrm{m}} = n_{\mathrm{s}} n_{\mathrm{c}}$	number of measurements
n_{s}	number of samples per channel
n_{c}	number of channels
n_{p}	number of configuration parameters per frame
n_{f}	number of frames
n_μ	number of chromophores
n_λ	number of optical wavelengths

optical properties from each other. In multi-wavelength imaging, this enables visualization of molecular tissue contrast. The tissue optical absorption μ_{a} is determined by a weighted linear combination

$$\mu_{\mathrm{a}}(\lambda, \mathbf{r}) = \sum_i m_i(\lambda)\, \chi_i(\mathbf{r}), \tag{3}$$

where $m_i(\lambda)$ is the optical absorption at wavelength λ, for the i-th chromophore, and $\chi_i(\mathbf{r})$ is its *volume fraction abundance*.

In an acoustically homogeneous medium, pressure waves due to $\psi(\mathbf{r}, \lambda)$ propagate radially outward from $\mathbf{r}$ at a constant speed of sound c_0. The signal measured by an acoustic transducer at position $\mathbf{r}_0$, at time t, is

$$y(\lambda, \mathbf{r}_0, t) = \int_{\mathbb{R}^3} h(\mathbf{r}_0 - \mathbf{r}, t)\, \psi(\lambda, \mathbf{r})\ \mathrm{d}\mathbf{r}. \tag{4}$$

Here, the *spatio-temporal impulse response* for a transducer measurement is

$$h(\mathbf{r}, t) = \int_{-\infty}^{\infty} \int_{\mathbb{R}^3} g'(\tilde{\mathbf{r}}, \tilde{t}) f_{\mathbf{a}}(\mathbf{r} - \tilde{\mathbf{r}}) \alpha(\tilde{\mathbf{r}}) \beta(t - \tilde{t})\ \mathrm{d}\tilde{\mathbf{r}}\ \mathrm{d}\tilde{t}, \tag{5}$$

where

$$g'(\mathbf{r}, t) = \frac{\partial}{\partial t} \frac{\delta\left(\|\mathbf{r}\| - c_0 t\right)}{4\pi t} \tag{6}$$

is the *ideal impulse response* for an infinitesimally-sized omni-directional transducer. In this equation, $\delta(t)$ is the Dirac delta function. In (5), the *transducer aperture function* $f_{\mathbf{a}}(\mathbf{r})$ models the element geometry. For rectangular elements, this is

$$f_{\mathbf{a}}(\mathbf{r}) = \mathrm{rect}\left(\frac{r_1}{a_1}, \frac{r_2}{a_2}\right) \delta(r_3), \tag{7}$$

where a_1 and a_2 represent the element length and width, and the element is oriented normal to the r_3-axis, with coordinates $\mathbf{r} = (r_1, r_2, r_3)$. The *obliquity factor*

$$\alpha(\mathbf{r}) = \frac{|\mathbf{r} \cdot \hat{\mathbf{n}}|}{\|\mathbf{r}\|} \tag{8}$$

models the transducer directionality. Here, $\hat{\mathbf{n}}$ is the outward normal to the transducer at $\mathbf{r}$. For an omni-directional transducer, which does not include directionality, $\alpha(\mathbf{r})$ is set to 1. The *electro-mechanical impulse response* $\beta(t)$ describes the spatially-independent bandwidth of the receiving element and system electronics. To model an ideal wide-band response, where $\beta(t)$ has no contribution, $\beta(t)$ can be set to $\delta(t)$.

B. Image Reconstruction Using Mathematical Optimization

Images of tissue can be reconstructed from acquired sensor measurements using mathematical optimization algorithms [22], [23], [23]–[27], [46]–[58]. This involves finding an unknown $\mathbf{x}$ that minimizes error between a *measured response* $\mathbf{y}$ and a *predicted response* $\tilde{\mathbf{y}} = H\mathbf{x}$. Here, the *system matrix* H models the responses that are predicted to be measured for any given image $\mathbf{x}$. Representing the response of a linear system by H generally involves converting continuous equations to discretized matrix form. For example, H can implement transducers using equation (5) to model an OA system, as detailed in Section III-B to represent our model.

To solve $\mathbf{x}$, a general approach that covers many applications in image and signal processing [47]–[50], [53]–[55] involves minimizing a convex optimization problem of the form

$$\begin{aligned} &\text{minimize} \quad \|H\mathbf{x} - \mathbf{y}\|_2^2 + \vartheta(\mathbf{x}) \\ &\text{subject to} \quad \mathbf{x} \in \mathcal{C} \end{aligned} \tag{9}$$

When an optimization problem is convex, its *global optimal solution* can be found iteratively by computing a converging sequence of solutions. Here, $\|H\mathbf{x} - \mathbf{y}\|_2^2$ is a *fidelity function* that matches measured data to the model. The *regularization function* $\vartheta(\mathbf{x})$ penalizes unwanted solutions, occurring due to noise amplification, which otherwise might minimize (9). Different regularization functions can be used depending on anticipated properties of the reconstructed image. Generally, $\vartheta(\mathbf{x})$ has a corresponding *proximal operator* that can be computed efficiently, as described in Appendix A. For example, in ℓ_1-minimization, $\vartheta(\mathbf{x})$ promotes sparse solutions, with few non-zero elements, by using an ℓ_1-norm $\|\cdot\|_1$. The ℓ_1 proximal operator is a simple soft-thresholding function. Our approach uses total-variation (TV) regularization [27], [48], [49], which involves a weighted ℓ_1-norm to enforce sparseness in the spatial gradient of $\mathbf{x}$, promoting image smoothness. This helps to reduce noise when visualizing tissue. In equation (9), the convex set $\mathcal{C}$ represents *constraints*, restricting the allowed values of $\mathbf{x}$. For example, $\mathcal{C} = \{x \,|\, x \geq 0\}$ will permit only non-negative values in $\mathbf{x}$, which is useful when the unknown variable must be positive.

Equation (9) can be solved by several techniques, including the alternating direction method of multipliers (ADMM) [52], [55], and accelerated proximal gradient (APG) [27], [47]–[50], [53]–[55]. Mathematical details of these minimization algorithms, as used in our approach, are provided in Appendix A.

To perform motion tracking, additional variables representing probe position and orientation must be solved. When these are included, the system matrix H becomes non-linear (with respect to these variables), which makes solving equation (9) more difficult compared to conventional image reconstruction. In this case, *sequential convex optimization* [42]–[45], [59], [60] can be used, which iteratively computes a sequence of linearized convex subproblems, as described in Section IV-C.

III. System Model

A. Frames Collected by Linear Array

In this work, a system model is developed by extending equation (4) to multiple frames. This is applicable in 2D clinical imaging, where a hand-held probe with linear transducer array is manually scanned along the surface of a subject's tissue. The probe delivers light through an *optical source aperture* (e.g. a transparent window) adjacent to the array. Following illumination by an optical pulse, the array records acoustic signals to capture a *frame* of data. In 2D imaging, each frame corresponds with a tissue slice in the probe's *imaging plane*. Figure 1 illustrates frames acquired at two alternating wavelengths along the probe's trajectory.

By extending equation (4), the opto-acoustic signals for the j-th frame are

$$y_j(\mathbf{r}_l, t) = \int_{\mathbb{R}^3} h(\mathbf{r}_l - \mathbf{r}, t)\, \psi_j(\mathbf{r})\ \mathrm{d}\mathbf{r}, \tag{10}$$

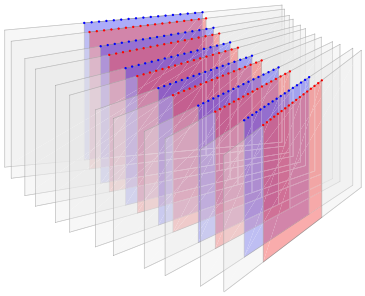

Fig. 1. Illustration of (dual-wavelength) multi-frame acquisition. Frames at alternating optical wavelengths λ_1 (red) and λ_2 (blue) are acquired as linear array transducer follows a trajectory at the surface of a subject's tissue (not shown). Transducer elements are shown as dots at the tissue surface.

where $\mathbf{r}_l$ is the position of the l-th transducer element in the probe's local coordinate system, and t is time elapsed since illumination. Since the probe can move, the frame's acoustic source distribution ψ_j is defined relative to the probe's coordinates, and depends on the probe's illumination of tissue. This is equal to

$$\psi_j(\mathbf{r}) = \eta(\lambda_j, \tau_j(\mathbf{r}))\, \varphi(\lambda_j, \mathbf{r}), \tag{11}$$

where the rotation and translation for each frame are represented using a rigid *affine transform function*

$$\tau_j(\mathbf{r}) = A_j \mathbf{r} + \mathbf{b}_j, \tag{12}$$

with rotation matrix A_j and translation $\mathbf{b}_j$. Thus, τ_j converts η from global coordinates to the probe's local coordinates. In global coordinates, by combining (2) and (3), η is given by

$$\eta(\lambda_j, \mathbf{r}) = \gamma(\mathbf{r}) \sum_i m_i(\lambda_j)\, \chi_i(\mathbf{r}), \tag{13}$$

where λ_j is the optical wavelength of the j-th frame. In a dual-wavelength system, λ_j sequentially alternates between two different values. Since the optical source aperture moves with the probe, the light distribution φ is assumed to remain stationary in the probe's coordinates.

B. Forward Model

The forward model predicts the data received by the probe. In equations (10) to (13), the opto-acoustic signals y_j depend on: i) the volume fraction abundances χ_i, for chromophores $i = 1, \ldots, n_\mu$; and, ii) the probe's orientation A_j and position $\mathbf{b}_j$, for frames $j = 1, \ldots, n_\mathrm{f}$. These parameters correspond to inputs in our forward model, but also represent the unknown variables solved during image reconstruction. The other parameters, m_i, φ and γ, are treated as constants that are determined in advance.

1) Volume Fraction Abundance of Chromophores in Tissue: To model the tissue, it is subdivided into voxels, arranged on a 3D grid. Each voxel is associated with a set of chromophore abundances. The total number of voxels is $n_\mathrm{v} = n_\mathrm{x} n_\mathrm{y} n_\mathrm{z}$, where n_x, n_y and n_z are the number of voxels along the x-, y- and z-axes. For the i-th chromophore, the volume fraction abundance is represented as a vector $\mathbf{x}_i \in \mathbb{R}^{n_\mathrm{v}}$. Thus, the tissue can be represented by a matrix variable $X = [\mathbf{x}_1, \mathbf{x}_2, \ldots, \mathbf{x}_{n_\mu}] \in \mathbb{R}^{n_\mathrm{v} \times n_\mu}$, where n_μ is the number of chromophores. For convenience, this is vectorized to $\mathbf{x} = \mathrm{vec}(X) \in \mathbb{R}^{n_\mathrm{v} n_\mu}$.

2) System Matrix: For a tissue represented by $\mathbf{x} \in \mathbb{R}^{n_\mathrm{v} n_\mu}$, the predicted opto-acoustic signals for the j-th frame are represented by a vector $\tilde{\mathbf{y}}_j \in \mathbb{R}^{n_\mathrm{m}}$. The number of measurements n_m is equal to the number of transducer channels n_c times the number of samples per channel n_s. For each frame, a *system matrix* $H_j \in \mathbb{R}^{(n_\mathrm{m}) \times (n_\mathrm{v} n_\mu)}$ is used to represent the linear discretized operator corresponding to equation (10). Thus, the predicted response is

$$\tilde{\mathbf{y}}_j = H_j \mathbf{x}.$$

In our model, the operator H_j, which is composed of four components, is defined as

$$H_j = H_0\, \Phi_{\lambda_j}\, T_{\mathbf{p}_j}\, M_{\lambda_j}, \tag{14}$$

where $M_{\lambda_j} \in \mathbb{R}^{(n_\mathrm{v}) \times (n_\mathrm{v} n_\mu)}$ is the *absorption matrix* for wavelength λ_j, which contains optical absorption coefficients of each chromophore; $T_{\mathbf{p}_j} \in \mathbb{R}^{n_\mathrm{v} \times n_\mathrm{v}}$ is the *transformation matrix* for the configuration vector $\mathbf{p}_j \in \mathbb{R}^{n_\mathrm{p}}$, which describes probe position and orientation; $\Phi_{\lambda_j} \in \mathbb{R}^{n_\mathrm{v} \times n_\mathrm{v}}$ is the *optical illumination matrix* for wavelength λ_j, describing the radiant fluence distribution; and, $H_0 \in \mathbb{R}^{n_\mathrm{m} \times n_\mathrm{v}}$ is the *acoustic response matrix*. These are described below.

To compute signals from multiple frames, the *overall system matrix* $H \in \mathbb{R}^{(n_\mathrm{m} n_\mathrm{f}) \times (n_\mathrm{v} n_\mu)}$ is given by

$$H = \begin{bmatrix} H_1 \\ H_2 \\ \vdots \\ H_{n_\mathrm{f}} \end{bmatrix}. \tag{15}$$

Thus, we can write

$$\tilde{\mathbf{y}} = H \mathbf{x}, \tag{16}$$

where $\tilde{Y} = [\tilde{\mathbf{y}}_1, \tilde{\mathbf{y}}_2, \ldots, \tilde{\mathbf{y}}_{n_\mathrm{f}}] \in \mathbb{R}^{n_\mathrm{m} \times n_\mathrm{f}}$ and $\tilde{\mathbf{y}} = \mathrm{vec}(\tilde{Y})$.

3) Absorption Matrix (M_{λ_j}): To derive M_{λ_j}, equation (13) is used. It is assumed that each chromophore index $i \in \{1, \ldots, n_\mu\}$ has a known absorption coefficient $m_i(\lambda_j)$ at the wavelength index $\lambda_j \in \{1, \ldots, n_\lambda\}$. We define the *optical absorption vector* $\mathbf{m}_{\lambda_j} \in \mathbb{R}^{n_\mu}$ at wavelength λ_j as

$$\mathbf{m}_{\lambda_j} = \left[m_1(\lambda_j), m_2(\lambda_j), \ldots, m_{n_\mu}(\lambda_j) \right]^T. \tag{17}$$

Next, by applying equation (13) in matrix form, the abundance matrix $X \in \mathbb{R}^{n_\mathrm{v} \times n_\mu}$ can be used to find the opto-acoustic conversion efficiency by computing

$$\Gamma X \mathbf{m}_{\lambda_j}. \tag{18}$$

Here, $\Gamma \in \mathbb{R}^{n_\mathrm{v} \times n_\mathrm{v}}$ is a diagonal matrix, representing the Grüneisen parameter $\gamma(\mathbf{r})$, which applies pointwise multiplication to each voxel. To reorder (18), we use the vectorization identity, $\mathrm{vec}(UV) = (V^T \otimes I_k)\, \mathrm{vec}(U)$, which is valid for any matrices $U \in \mathbb{R}^{k \times l}$ and $V \in \mathbb{R}^{l \times m}$, where I_k represents the size k identity matrix and $\otimes$ is a Kronecker tensor product. This yields $\Gamma X \mathbf{m}_{\lambda_j} = \Gamma (\mathbf{m}_{\lambda_j}^T \otimes I_{n_\mathrm{v}})\, \mathrm{vec}(X)$. Accordingly, we can write (18) as a matrix operator that is applied to $\mathbf{x} = \mathrm{vec}(X)$. Also, for simplicity, we assume that $\gamma(\mathbf{r})$ does not vary spatially, and is represented by a constant γ_0, such that $\Gamma = \gamma_0 I_{n_\mathrm{v}}$. Therefore, the optical absorption matrix for (14) is given by

$$M_{\lambda_j} = \tilde{\mathbf{m}}_{\lambda_j}^T \otimes I_{n_\mathrm{v}}, \tag{19}$$

where $\tilde{\mathbf{m}}_{\lambda_j} = \gamma_0\, \mathbf{m}_{\lambda_j}$. This has a simple interpretation, which is that equation (19) replicates $\mathbf{m}_{\lambda_j}$ for each voxel and multiplies by γ_0.

4) Transformation Matrix ($T_{\mathbf{p}_j}$): In each frame, the probe has a different position and orientation. The rotation matrix $A_j \in \mathbb{R}^{3\times3}$ and the translation $\mathbf{b}_j \in \mathbb{R}^3$ of equation (12) can be generated by a list of parameters $\mathbf{p}_j \in \mathbb{R}^{n_\mathrm{p}}$ called the *configuration*. There is some flexibility in how A_j and $\mathbf{b}_j$ are generated from the configuration, depending on the permitted probe motions. The number of parameters n_p is equal to the degrees of freedom. We use the configuration $\mathbf{p}_j = (\boldsymbol{\theta}_j, \mathbf{b}_j)$, which has six parameters: the three translations for $\mathbf{b}_j$, and three Euler angles $\boldsymbol{\theta}_j \in \mathbb{R}^3$ to represent roll, pitch and yaw. The rotation matrix is

$$A_j = R_1(\theta_{j,1})\, R_2(\theta_{j,2})\, R_3(\theta_{j,3}), \tag{20}$$

where R_1, R_2 and R_3 represent rotations about the three coordinate axes. If fewer degrees of freedom are required, then any of the configuration parameters can be replaced with constants to constrain the trajectory.

In earlier work [28], we described probe orientation A_j and position $\mathbf{b}_j$, and the conversion between different coordinates. Here, we define the transformation matrix $T_{\mathbf{p}_j} \in \mathbb{R}^{n_\mathrm{v}\times n_\mathrm{v}}$ for (14) as an operator that transforms voxels in $\mathbb{R}^{n_\mathrm{v}}$ according to the configuration $\mathbf{p}_j$. In other words, $T_{\mathbf{p}_j}$ applies A_j and $\mathbf{b}_j$ to each voxel in an image. This (inversely) rotates and translates the tissue so it is situated in the local coordinate frame of the probe. In practice, the matrix $T_{\mathbf{p}_j}$ can be implemented efficiently using a custom function on a CPU or GPU.

5) Optical Illumination Matrix (Φ_{λ_j}): In our model, light is delivered by an optical aperture that remains stationary in the probe's local coordinates. Thus, for wavelength λ_j, it is assumed the fluence profile φ remains fixed relative to the probe. This permits pre-computing Φ once per wavelength, rather than solving it at each probe position. As described in our earlier work [28], this approximation assumes tissue heterogeneities and deformation that impact φ are negligible. According to equation (1), the optical illumination matrix $\Phi_{\lambda_j} \in \mathbb{R}^{n_\mathrm{v}\times n_\mathrm{v}}$ must apply a diagonal weighting, corresponding to pointwise multiplication of each voxel. Thus, $\Phi_{\lambda_j} = \mathrm{diag}(\boldsymbol{\varphi}_{\lambda_j})$, where $\boldsymbol{\varphi}_{\lambda_j} \in \mathbb{R}^{n_\mathrm{v}}$ is a vector representing the fluence profile. This is governed by the radiation transport equation and can be determined in several ways, including diffusion approximations [61]–[64], finite-element models [65], or Monte Carlo based methods [66], [67]. Our implementation uses analytic expressions based on the diffusion approximation [28], [63] with optical properties for breast tissue [4].

6) Acoustic Response Matrix (H_0): The acoustic response matrix $H_0 \in \mathbb{R}^{n_\mathrm{m}\times n_\mathrm{v}}$ implements equation (5) in linear discretized form, as described in the next section.

C. Separable Operator for Linear Array

In earlier work [28], we proved that a mathematical operator corresponding to equations (10) to (12) is separable. For each transducer, this implements the spherical volume integration of equations (4) to (6) to model acoustic wave propagation in a more efficient manner. By generalizing this to matrix form, the acoustic response matrix $H_0 \in \mathbb{R}^{n_\mathrm{m}\times n_\mathrm{v}}$ can be represented as the product of two matrices. This is written[1]

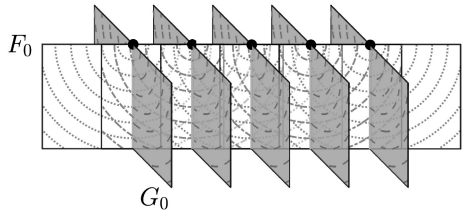

Fig. 2. Separable acoustic response matrix [28]. To improve computational efficiency for a linear array, the response matrix $H_0 = F_0\, G_0$ performs spherical volume integration of equation (5) in two stages. To model time-domain signals for all transducer elements (black dots), the matrix factor F_0 integrates along arcs that span a 2D plane (white) corresponding to a cross-sectional slice of tissue. The slice is generated by the matrix factor G_0, which integrates along independent perpendicular planes (gray), spanning the 3D volume. Since the transducer elements are co-linear, all signals in F_0 require the same planes from G_0 (repeated at consecutive offsets as shown), so intermediate data can be shared. Thus, by splitting H_0 into factors F_0 and G_0, redundant computation is eliminated.

$$H_0 = F_0\, G_0. \tag{21}$$

Here, the matrix factor $F_0 \in \mathbb{R}^{n_\mathrm{m}\times n_{\mathrm{m}'}}$ acts on the probe's 2D imaging plane. The factor $G_0 \in \mathbb{R}^{n_{\mathrm{m}'}\times n_\mathrm{v}}$ acts along planes perpendicular to it, spanning a 3D volume. This is illustrated in Figure 2. In the matrices, the intermediate number of measurements $n_{\mathrm{m}'}$ is different from n_m.

By representing (21) as sparse matrices, the separable form permits higher computational efficiency because H_0 is non-factorized and less sparse than F_0 and G_0. The performance improvement for factorized sparse matrices is similar to the case for discretized analytic equations (described in our earlier work [28]) because the sparsity pattern yields the same number of operations.

We can apply separability to the overall system matrix H of equation (15). By substituting (21) into (14), for frame j, we have

$$H_j = F_0 \underbrace{G_0\, \Phi_{\lambda_j}\, T_{\mathbf{p}_j}\, M_{\lambda_j}}_{G_j}, \tag{22}$$

where G_j is defined as

$$G_j = G_0\, \Phi_{\lambda_j}\, T_{\mathbf{p}_j}\, M_{\lambda_j}. \tag{23}$$

Accordingly, (15) can be written as

$$H = F\, G, \tag{24}$$

where the overall separable factors F and G are

$$F = F_0 \otimes I_{n_\mathrm{f}} = \begin{bmatrix} F_0 & 0 & \cdots & 0 \\ 0 & F_0 & \cdots & 0 \\ \vdots & \vdots & \ddots & \vdots \\ 0 & 0 & \cdots & F_0 \end{bmatrix}, \tag{25}$$

[1]The matrix equation $H_0 = F_0\, G_0$ corresponds to the compositionally separable operator $\mathcal{H} = \tilde{\mathcal{G}} \circ \mathcal{G}$, which is described in [28] .

and

$$G = \begin{bmatrix} G_1 \\ G_2 \\ \vdots \\ G_{n_\mathrm{f}} \end{bmatrix}. \tag{26}$$

Using the separable form of equation (24) (instead of performing a volume integration that encounters each voxel for every transducer), reduces the computational complexity of each frame from $\mathcal{O}(n^3)$ to approximately $\mathcal{O}(n^2)$, where $n^3 = n_\mathrm{v}$ is the number of voxels in a 3D image (assuming the number of transducers $n_\mathrm{c} \approx n$) [28]. For a 3D image with dimensions $100 \times 100 \times 100$, this represents 100 times computational savings, compared to a non-separable approach.

IV. Image Reconstruction and Motion Tracking

A. Image Reconstruction

Image reconstruction using the separable operator described in Section III-C is performed by substituting (15) into (9) to obtain the convex optimization problem

$$\begin{aligned} &\underset{\mathbf{x}}{\text{minimize}} \quad \|FG\mathbf{x} - \mathbf{y}\|_2^2 + \vartheta(\mathbf{x}) \\ &\text{subject to} \quad \mathbf{x} \in \mathcal{C} \end{aligned} \tag{27}$$

Here $\mathbf{x}$ represents the volume fraction abundances of the tissue chromophores, which have non-negative values. Accordingly, our implementation specifies $\mathcal{C}$ with $\mathbf{x} \geq 0$. To solve (27), we use a minimization algorithm [53], [55] that requires a proximal operator of the indicator function $\mathcal{I}_\mathcal{C}$ to confine $\mathbf{x}$ to $\mathcal{C}$. This corresponds to a simple replacement of negative values with zero after each iteration. If desired, additional constraints can be used, such as ensuring the volume fractions sum to less than one, consistent with physical principles. An overview of constraints used in optimization-based spectral unmixing is provided by Chouzenoux et al. [68].

When solving (27), we used a regularization function ϑ that included isotropic TV as well as ℓ_1-minimization. Our implementation specified

$$\vartheta(\mathbf{x}) = \alpha_1 \|\mathbf{x}\|_1 + \alpha_2 \sum_{i=1}^{n_\mu} \|D\mathbf{x}_i\|_{2,1}, \tag{28}$$

where α_1 and α_2 are regularization parameters, and $D = (D_x, D_y, D_z) \in \mathbb{R}^{(3\times n_\mathrm{v})\times n_\mathrm{v}}$ is a linear matrix operator for TV regularization that computes spatial gradients in the x, y and z directions. Here, D is applied to each chromophore $\mathbf{x}_i$. In equation (28), the $\|\cdot\|_{2,1}$ group-norm has a dual-proximal operator that facilitates using isotropic TV with 3D volumes. Minimizing this type of equation can be performed efficiently with dual-proximal methods, such as TFOCS [53], [57] (as described in Appendix A), or by using similar approaches involving primal-dual optimization [56]. If desired, anisotropic TV can be implemented by using the ℓ_1-norm $\|\cdot\|_1$ in (28) instead of $\|\cdot\|_{2,1}$, which may reduce visual performance, but is computationally simpler.

B. Two-Stage Iterative 3D Opto-Acoustic Image Reconstruction

To improve computation of equation (27), a two-stage iterative 3D reconstruction is proposed, where separable parts are solved independently. The sequence, which is performed iteratively, involves first reconstructing a monochrome (single-wavelength) 2D slice for each frame, followed by 3D volumetric reconstruction of chromophores.

Using the separable operator of Section III-C, equation (27) is split into two parts. From (22) and (23), when H_j is applied to $\mathbf{x}$, we can write

$$H_j\mathbf{x} = F_0 \underbrace{G_j\mathbf{x}}_{\mathbf{z}_j} = F_0\,\mathbf{z}_j, \tag{29}$$

where $\mathbf{z}_j \in \mathbb{R}^{n_{\mathrm{m}'}}$ is a new variable, defined by

$$\mathbf{z}_j = G_j\mathbf{x}. \tag{30}$$

We write $Z = [\mathbf{z}_1, \ldots, \mathbf{z}_{n_\mathrm{f}}] \in \mathbb{R}^{n_{\mathrm{m}'}\times n_\mathrm{f}}$ and $\mathbf{z} = \mathrm{vec}(Z)$. Thus, for the overall system matrix,

$$H\mathbf{x} = FG\mathbf{x} = F\mathbf{z}, \tag{31}$$

where $G\mathbf{x} = \mathbf{z}$. Using this substitution, equation (27) becomes

$$\begin{aligned} &\underset{\mathbf{x},\mathbf{z}}{\text{minimize}} \quad \|F\mathbf{z} - \mathbf{y}\|_2^2 + \vartheta(\mathbf{x}) \\ &\text{subject to} \quad \mathbf{z} = G\mathbf{x}, \end{aligned} \tag{32}$$

where the constraint $\mathbf{x} \in \mathcal{C}$ is omitted for clarity.

Equation (32) can be solved with the ADMM splitting algorithm, as described in Appendix A. The result obtained by applying (32) to (A.5) is presented as Algorithm 1. An interesting interpretation of Algorithm 1 is that there is an intermediate variable $\mathbf{z}_j$ for each frame, corresponding to a monochrome 2D reconstructed image. Each reconstructed $\mathbf{z}_j$ requires no inherent positional information, since it is in the probe's local coordinates. Algorithm 1 performs an outer loop, with two separate inner minimizations. First, the algorithm reconstructs a 2D image $\mathbf{z}_j$ for each frame. Then, once $\mathbf{z}_j$ is formed for all frames, the 3D volume $\mathbf{x}$ is reconstructed from the intermediate variables, using each frame's position and orientation. Since the positional information is not required until the second stage, motion tracking can be solved using data computed from the first stage, as described in Section IV-C.

C. Image Reconstruction Combined With Motion Tracking

Motion tracking is developed from equation (9), using the system matrix H of equation (15), which depends on the configuration parameters $\mathbf{p} = (\mathbf{p}_1, \ldots, \mathbf{p}_{n_\mathrm{f}})$ that describe the probe orientation and position for each frame. To highlight the non-linear dependence of H on $\mathbf{p}$, we write the system matrix as $H \equiv H_\mathbf{p}$. To simultaneously perform reconstruction of $\mathbf{x}$, while determining probe configuration $\mathbf{p}$, it is desirable to solve

$$\underset{(\mathbf{x},\,\mathbf{p})\in\mathcal{C}}{\text{minimize}} \quad \|H_\mathbf{p}\,\mathbf{x} - \mathbf{y}\|_2^2 + \vartheta(\mathbf{x}) \tag{33}$$

However, due to the form of $H_\mathbf{p}$, which is non-linear in $\mathbf{p}$, equation (33) is not convex, which makes finding a solution difficult.

To convert (33) to a form that can be solved, a linear approximation to $H_\mathbf{p}$ around an initial estimate of $\mathbf{p}$ is used. For an incremental change in configuration parameters $\Delta\mathbf{p} \in \mathbb{R}^{(n_\mathrm{p} n_\mathrm{f})}$,

Algorithm 1: Two-Stage Iterative 3D Opto-Acoustic Image Reconstruction.

Input: $\mathbf{y} = (\mathbf{y}_1, \ldots, \mathbf{y}_{n_\mathrm{f}}) \in \mathbb{R}^{n_\mathrm{f} n_\mathrm{m}}$
Output: $\mathbf{x} \in \mathbb{R}^{n_\mathrm{v} n_\mu}$
Require: $F_0 \in \mathbb{R}^{n_{n_\mathrm{m} \times \mathrm{m}'}}$, $G = (G_1, \ldots, G_{n_\mathrm{f}}) \in \mathbb{R}^{n_\mathrm{f} n_{\mathrm{m}'} \times n_\mathrm{v} n_\mu}$, $\vartheta : \mathbb{R}^{n_\mathrm{v} n_\mu} \to \mathbb{R}$, $\rho \in \mathbb{R}^+$

function TWO STAGE RECONSTRUCT($\mathbf{y}_1, \ldots, \mathbf{y}_{n_\mathrm{f}}$)
  $\mathbf{x}^{(0)} \leftarrow 0$, $\mathbf{u}^{(0)} \leftarrow 0$ ▷ Initialize $\mathbf{x}$ and $\mathbf{u}$
  for $n = 0 \ldots n_{\max} - 1$ **do**
    for $j = 1 \ldots n_\mathrm{f}$ **do** ▷ Perform 2D reconstruction for each slice
      $\mathbf{z}_j^{(n+1)} \leftarrow$ RECONSTRUCT2D($\mathbf{y}_j$, $G_j \mathbf{x}^{(n)} + \mathbf{u}_j^{(n)}$)
    end for
    $\mathbf{z}^{(n+1)} \leftarrow (\mathbf{z}_1^{(n+1)}, \mathbf{z}_2^{(n+1)}, \ldots, \mathbf{z}_{n_\mathrm{f}}^{(n+1)})$
    $\mathbf{x}^{(n+1)} \leftarrow$ RECONSTRUCT3D ($\mathbf{z}^{(n+1)} - \mathbf{u}^{(n)}$) ▷ Reconstruct 3D volume using all slices
    for $j = 1 \ldots n_\mathrm{f}$ **do** ▷ Update dual variables
      $\mathbf{u}_j^{(n+1)} \leftarrow \mathbf{u}_j^{(n)} + (G_j \mathbf{x}^{(n+1)} - \mathbf{z}_j^{(n+1)})$
    end for
    $\mathbf{u}^{(n+1)} \leftarrow (\mathbf{u}_1^{(n+1)}, \mathbf{u}_2^{(n+1)}, \ldots, \mathbf{u}_{n_\mathrm{f}}^{(n+1)})$
  end for
  return $\mathbf{x}^{(n+1)}$
end function
function RECONSTRUCT2D($\mathbf{y}_0, \mathbf{u}_0$)
  return $\underset{\mathbf{z}_0}{\operatorname{argmin}} \{\|F_0 \mathbf{z}_0 - \mathbf{y}_0\|_2^2 + \frac{\rho}{2} \|\mathbf{u}_0 - \mathbf{z}_0\|_2^2\}$
end function
function RECONSTRUCT3D($\tilde{\mathbf{z}}$)
  return $\underset{\mathbf{x}}{\operatorname{argmin}} \{\frac{\rho}{2} \|G\mathbf{x} - \tilde{\mathbf{z}}\|_2^2 + \vartheta(\mathbf{x})\}$ ▷ 3D volumetric recontruction of chromophores
end function

Algorithm 2: Opto-Acoustic Image Reconstruction with Motion Tracking

Input: $\mathbf{y} = (\mathbf{y}_1, \ldots, \mathbf{y}_{n_\mathrm{f}}) \in \mathbb{R}^{n_\mathrm{f} n_\mathrm{m}}$
Output: $\mathbf{x} \in \mathbb{R}^{n_\mathrm{v} n_\mu}$, $\mathbf{p} \in \mathbb{R}^{n_\mathrm{p} n_\mathrm{f}}$

procedure: RECONSTRUCTIONANDTRACKING($\mathbf{y}$)
  $\mathbf{x}^{(0)} \leftarrow 0$, $\mathbf{p}^{(0)} \leftarrow 0$ ▷ Initialize $\mathbf{x}$ and $\mathbf{p}$
  for $k = 0 \ldots k_{\max} - 1$ **do**
    for $j = 1 \ldots n_\mathrm{f}$ **do**
      $H_{\mathbf{p}_j}^{(k)} \leftarrow H_0 \, \Phi_{\lambda_j} \, T_{\mathbf{p}_j}^{(k)} \, M_{\lambda_j}$ ▷ Update the system response of frame j from (14)
      $J_{\mathbf{p}_j}^{(k)} \leftarrow \frac{\partial H_{\mathbf{p}_j}^{(k)} \mathbf{x}^{(k)}}{\partial \mathbf{p}_j}\big|_{\mathbf{p}_j^{(k)}}$ ▷ Update Jaccobian of frame j
    end for
    $(\mathbf{x}^{(k+1)}, \Delta\mathbf{p}^{(k+1)}) \leftarrow \underset{(\mathbf{x}, \Delta\mathbf{p}) \in \mathcal{C}_k}{\operatorname{argmin}} \{\|H_{\mathbf{p}}^{(k)} \mathbf{x} + J_{\mathbf{p}}^{(k)} \Delta\mathbf{p} - \mathbf{y}\|_2^2 + \vartheta(\mathbf{x})\}$ ▷ Update $\mathbf{x}$ and $\Delta_{\mathbf{p}}$ from (34a)
    $\mathbf{p}^{(k+1)} \leftarrow \mathbf{p}^{(k)} + \Delta\mathbf{p}^{(k+1)}$ ▷ Update $\mathbf{p}$ from (34b)
  end for
end procedure

the linear approximation is

$$H_{(\mathbf{p}+\Delta\mathbf{p})} \approx H_{\mathbf{p}} + J_{\mathbf{p}} \, \Delta\mathbf{p},$$

where $J_{\mathbf{p}} = \frac{\partial}{\partial \mathbf{p}}(H_{\mathbf{p}} \mathbf{x}) \in \mathbb{R}^{n_\mathrm{m} \times (n_\mathrm{p} n_\mathrm{f})}$ represents the Jaccobian derivative of $H_{\mathbf{p}}$ at $\mathbf{x}$ with respect to each parameter in $\mathbf{p}$. This permits iteratively solving a relaxed approximation to (33), where each iteration is a two step process. This two step approach is known as sequential convex optimization. At the k-th iteration, first, solutions for $\mathbf{x}^{(k+1)}$ and $\Delta\mathbf{p}^{(k+1)}$ are simultaneously solved. Then, $\mathbf{p}^{(k+1)}$ is solved by incrementally updating $\mathbf{p}^{(k)}$ with $\Delta\mathbf{p}^{(k+1)}$. Thus, each iteration consists of the following two steps:

Step 1:

$$\begin{bmatrix} \mathbf{x}^{(k+1)} \\ \Delta\mathbf{p}^{(k+1)} \end{bmatrix} = \underset{(\mathbf{x}, \Delta\mathbf{p}) \in \mathcal{C}_k}{\operatorname{argmin}} \left\{ \|H_{\mathbf{p}}^{(k)} \mathbf{x} + J_{\mathbf{p}}^{(k)} \Delta\mathbf{p} - \mathbf{y}\|_2^2 + \vartheta(\mathbf{x}) \right\} \tag{34a}$$

Step 2:

$$\mathbf{p}^{(k+1)} = \mathbf{p}^{(k)} + \Delta\mathbf{p}^{(k+1)} \tag{34b}$$

This is illustrated in Algorithm 2.

To constrain for constant velocity motion estimation, $\mathcal{C}_k$ can project $\mathbf{p}^{(k)}$ onto a linear trajectory along the probe's elevational axis after each iteration using robust fitting.

D. Efficient Implementation of Reconstruction and Tracking

By combining separability of Section III-C with Algorithm 2, additional advantages can be achieved. For example, when a 2D slice is separately reconstructed using data from each frame, this can be used to determine an initial estimate of motion along the lateral axis of the probe. We modify equation (32) into a split form similar to equation (34a). The split form permits applying the Jacobian matrix $J_{\mathbf{p}}$ in the 2D image-domain of $\mathbf{z}$, rather than in the time-domain of measurement data $\mathbf{y}$, which leads to a more efficient implementation. With these modifications, our implementation of Step 1 becomes

$$\begin{aligned} \underset{\mathbf{x},\mathbf{z},\Delta\mathbf{p}}{\text{minimize}} \quad & \|F\mathbf{z}-\mathbf{y}\|_2^2 + \vartheta(\mathbf{x}) \\ \text{subject to} \quad & \mathbf{z} = G_{\mathbf{p}}^{(k)}\mathbf{x} + J_{\mathbf{p}}^{(k)}\Delta\mathbf{p}, \\ & \mathbf{x} \geq 0, \end{aligned} \tag{35}$$

where $\vartheta(\mathbf{x})$ is the same as equation (28).

As described in Appendix A, the TFOCS algorithm performs minimization using first-order iterations with an accelerated proximal gradient (APG) method [53], [69]. The approach can handle convex optimization problems in *block-composite form* (BCF), which is described in equation (A.6). However, to solve a problem in BCF form, it is manually converted to its dual form, described in equation (A.7). To represent equation (35) in BCF form, we use a primal variable $\mathbf{v} = (\mathbf{z}, \mathbf{x}, \Delta\mathbf{p})$. The result is illustrated in Algorithm 3, which combines Algorithm 1 with Algorithm 2. At the k-th (outer) iteration, the block-composite system matrix $L^{(k)}$ is

$$L^{(k)} = \begin{bmatrix} -1 & G_{\mathbf{p}}^{(k)} & J_{\mathbf{p}}^{(k)} \\ F & 0 & 0 \\ D & 0 & 0 \\ 1 & 0 & 0 \end{bmatrix}, \tag{36}$$

where D is the linear operator for TV regularization, as used in equation (28). The offset constant for (A.6) is $\mathbf{c} = (0, \mathbf{y}, 0, 0)$. To encode (35), the function map $\boldsymbol{\xi} = [\mathcal{I}_0, \|\cdot\|_2, \|\cdot\|_{2,1}, \|\cdot\|_1]$ is used, which implements $\vartheta(\mathbf{x})$. Here, $\mathcal{I}_0$ encodes the equality constraint. The proximal operator $\text{prox}_{\xi_0}(\mathbf{v})$ and dual-proximal operator $\text{prox}_{\boldsymbol{\xi}^*}(\mathbf{u})$, which are required in equation (A.7), are

$$\text{prox}_{\xi_0} = \begin{bmatrix} \text{prox}_{\mathcal{I}_{\mathbb{R}^n_+}} \\ \text{prox}_{\mathcal{I}_{\mathbb{R}^n_+}} \\ \text{prox}_{\mathcal{I}_{\mathbb{R}^n}} \end{bmatrix}, \quad \text{prox}_{\boldsymbol{\xi}^*} = \begin{bmatrix} \text{prox}_{\ell_2} \\ \text{prox}_{\mathcal{I}_{\mathbb{R}^n}} \\ \text{prox}_{\ell_{2,\infty}}(\alpha_2) \\ \text{prox}_{\ell_\infty}(\alpha_1) \end{bmatrix}. \tag{37}$$

Here, the function $\text{prox}_{\mathcal{I}_{\mathbb{R}^n_+}}$ represents projection into the positive halfspace $\mathbb{R}^n_+$, which implements the constraint $\mathbf{x} \geq 0$, replacing negative values with zero. The unconstrained primal variables are represented by $\text{prox}_{\mathcal{I}_{\mathbb{R}^n}}$. In (37), $\text{prox}_{\boldsymbol{\xi}^*}$ converts the remaining terms in equation (35) to dual form. Here, the ℓ_2-norm $\|\cdot\|_2$ is self-dual, so its dual-proximal operator is prox_{ℓ_2}; the ℓ_1 minimization term's dual is $\text{prox}_{\ell_\infty}$; and, dual for the $\|\cdot\|_{2,1}$ group-norm in (28) is $\text{prox}_{\ell_{2,\infty}}$. The constants α_1 and α_2 correspond to the regularization parameters in (28).

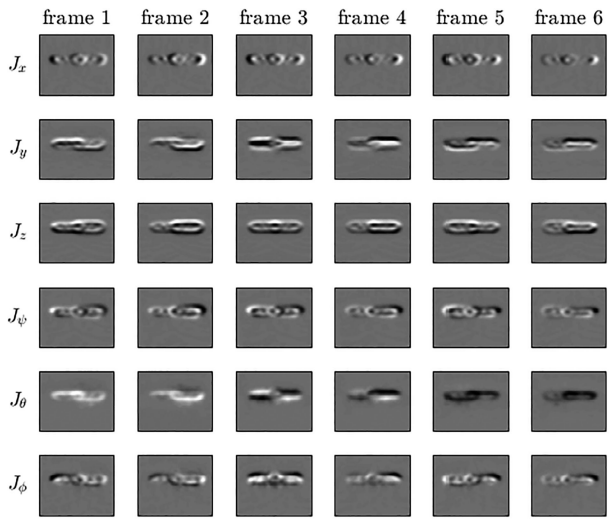

Fig. 3. Jacobian matrices for 6 acquired frames of digital phantom. The differences J_x, J_y, J_z, J_ψ, J_θ, and J_ϕ correspond to unit changes in $\mathbf{z}$ due to x, y, and z axis translations, roll, pitch, and yaw rotations.

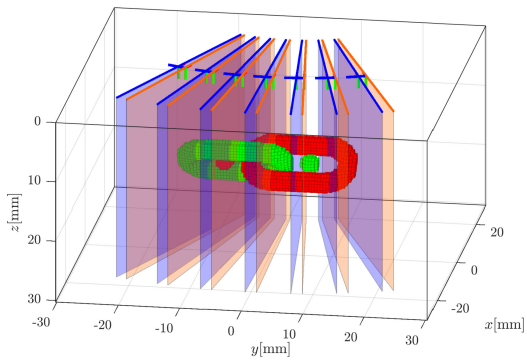

Fig. 4. A 3D digital phantom with chromophores oxy-hemoglobin (green) and deoxy-hemoglobin (red). The phantom contains two spheres and two links, arranged symmetrically and assigned opposite chromophores. The probe moves along a curved trajectory and acquires 14 OA frames with alternating optical wavelengths (represented by blue and orange planes). Position of linear array at tissue surface corresponds to blue and orange lines.

In Algorithm 3, at iteration k, the Jacobian matrix $J_{\mathbf{p}}^{(k)}$ can be computed by finite difference with respect to changes in $\mathbf{p}^{(k)}$. For illustration, Figure 3 shows $J_{\mathbf{p}}$, computed in the 2D image domain of $\mathbf{z}$, obtained from a digital phantom (described in Section V-A) using 6 frames. When solving equation (35), since the image $\mathbf{x}$ is initially unknown, $J_{\mathbf{p}}^{(0)}$ is initialized to zero and updated each iteration.

V. Results and Implementation

A. 3D Reconstruction of Digital Phantom

In this section, 3D multi-chromophore reconstruction is demonstrated using the digital phantom shown in Figure 4. To model different chromophores, the phantom contains inclusions consisting of oxy-hemoglobin (HbO_2) and deoxy-hemoglobin (HHb). The phantom's geometry is intended to be suggestive of a tumor, with a network of arteries and veins. Two spheres

Algorithm 3: Alternate Implementation of Image Reconstruction With Motion Tracking.

Input: $\mathbf{y} = (\mathbf{y}_1, \ldots, \mathbf{y}_{n_\mathrm{f}}) \in \mathbb{R}^{n_\mathrm{f} n_\mathrm{m}}$
Output: $\mathbf{x} \in \mathbb{R}^{n_v n_\mu}$, $\mathbf{p} \in \mathbb{R}^{n_\mathrm{f} n_\mathrm{p}}$
1: **procedure** RECONSTRUCTIONANDTRACKING($\mathbf{y}$)
2: $\mathbf{z}^{(0)} \leftarrow 0$, $\mathbf{x}^{(0)} \leftarrow 0$, $\mathbf{p}^{(0)} \leftarrow 0$ ▷ Initialize $\mathbf{z}$, $\mathbf{x}$ and $\mathbf{p}$
3: $\boldsymbol{\xi} \leftarrow \begin{bmatrix} \mathcal{I}_0 & \|\cdot\|_2 & \|\cdot\|_{2,1} & \|\cdot\|_1 \end{bmatrix}$
4: **for** $k = 0 \ldots k_{\max} - 1$ **do**
5: $$\begin{bmatrix} \mathbf{z}^{(k+1)} \\ \mathbf{x}^{(k+1)} \\ \Delta\mathbf{p}^{(k+1)} \end{bmatrix} \leftarrow \underset{(\mathbf{z},\mathbf{x},\Delta\mathbf{p}) \in \mathcal{C}_k}{\operatorname{argmin}} \left\{ \boldsymbol{\xi} \left(\begin{bmatrix} -1 & G_\mathbf{p}^{(k)} & J_\mathbf{p}^{(k)} \\ F & 0 & 0 \\ D & 0 & 0 \\ 1 & 0 & 0 \end{bmatrix} \begin{bmatrix} \mathbf{z} \\ \mathbf{x} \\ \Delta\mathbf{p} \end{bmatrix} - \begin{bmatrix} 0 \\ \mathbf{y} \\ 0 \\ 0 \end{bmatrix} \right) \right\}$$ ▷ Solve Eq. (35)
6: $\mathbf{p}^{(k+1)} \leftarrow \mathbf{p}^{(k)} + \Delta\mathbf{p}^{(k+1)}$ ▷ Update trajectory
7: **end for**
8: **end procedure**

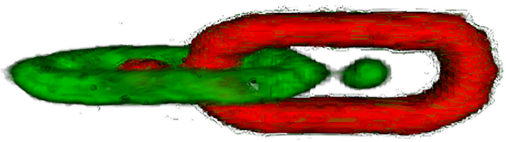

Fig. 5. 3D reconstruction of digital phantom of Figure 4.

and two links (ring shapes) of each chromophore are arranged symmetrically, as shown. The spheres have diameter 2 mm and are centered at depth 15 mm. The links are rotated $\pm 45^\circ$ about the z-axis, have a 2 mm ring-diameter, a major-axis length of 18 mm, and are centered at depth 15 mm.

Acquisition was modeled for a 2D OA probe with linear-array transducer. The illumination φ was pre-computed by assuming two rectangular optical apertures adjacent to the probe, with an effective optical attenuation for tissue of $\mu_{\text{eff}} = 1.2\ \text{cm}^{-1}$ at each wavelength. As shown in Figure 4, the probe follows a curved trajectory to acquire frames. Alternating 757 nm and 1064 nm optical pulses were modeled using a non-uniform pulse sequence, which involved a shorter delay after the first pulse than the second pulse. This type of sequence is used in conventional 2D image formation because motion artifacts are minimized by rapid acquisition of successive wavelengths, and the pulse repetition rate is limited by safety. Thus, our model includes frame positions that depend on probe trajectory as well as pulse timing.

The phantom was simulated with a 3D volume of $256 \times 256 \times 128$ voxels for each chromophore, with grid spacing 0.23 mm/voxel. Transducer elements were modeled using a line-aperture for $f_\mathbf{a}$ with 4 mm elevational width, cosine directionality α, and ideal electro-mechanical response β, per equation (5). A dataset of acoustic signals with added white noise was generated for 14 OA frames, as positioned in Figure 4.

For reconstruction, the minimization-based approach of equation (32) was used. The simulated dataset, along with probe position and orientation, served as input. The multi-chromophore reconstructed volume $X = [\mathbf{x}_1, \mathbf{x}_2]$ consisted of $(128 \times 128 \times 64) \times 2$ voxels, with grid spacing 0.3 mm/voxel, which is different from the simulated grid. A volume rendering of the reconstruction is shown in Figure 5, which displays $\mathbf{x}_2 - \mathbf{x}_1$ in a red/green palette to demonstrate chromophore reconstruction. Performance is considered in the next section.

B. Reconstruction and Motion Tracking Using Digital Phantom

To examine our approach for reconstruction and motion tracking, the multi-chromophore digital phantom of Section V-A was used. In the simulation, the OA probe was moved at constant velocity of 15 mm/s along its elevational axis, which was aligned with the y-coordinate of the phantom. Illumination alternated between 757 nm and 1064 nm wavelengths. A non-uniform pulse sequence was used with a 50 ms delay after the 757 nm wavelength and a 150 ms delay after the 1064 nm wavelength. A total of 14 frames were acquired at an average frame rate of 10 Hz.

Reconstruction was performed using Algorithm 3. The reconstructed volume had $(64 \times 64 \times 64) \times 2$ voxels, with grid spacing 0.6 mm/voxel. The variables $\mathbf{x}^{(k)}$ and $\mathbf{p}^{(k)}$ were stored after each outer iteration k. An initial velocity estimate of 25 mm/s was specified. There were 10 outer iterations performed, and each used 80 inner iterations. Reconstruction was implemented in Matlab using the TFOCS [69] solver. The system matrices F and G were computed by custom GPU functions [28] running on a GeForce GTX Titan with 3072 cores and 24 GB RAM. Total processing time was 1090 seconds. The results are shown in Figure 6, which illustrates the evolution of $\mathbf{x}^{(k)}$ after k iterations. As $\mathbf{p}^{(k)}$ becomes more accurate, the reconstructed 3D image improves. In the Supplemental Materials, Figure S-1 displays cross-sections of the volume as the reconstruction converges. The convergence of the normalized error of $\mathbf{x}^{(k)}$ and $\mathbf{p}^{(k)}$, relative to ground truth, is plotted in Figure S-2. Figure S-3 illustrates the evolution of the each frame's y-coordinate during the reconstruction.

C. Reconstruction From Clinical Data

An OA dataset of a fibroadenoma (a benign breast lesion) was acquired during a clinical feasibility study involving an investigational Imagio breast imaging system [3]. Using this dataset, reconstruction with the proposed technique was compared to 2D back-projection. The resulting images are shown

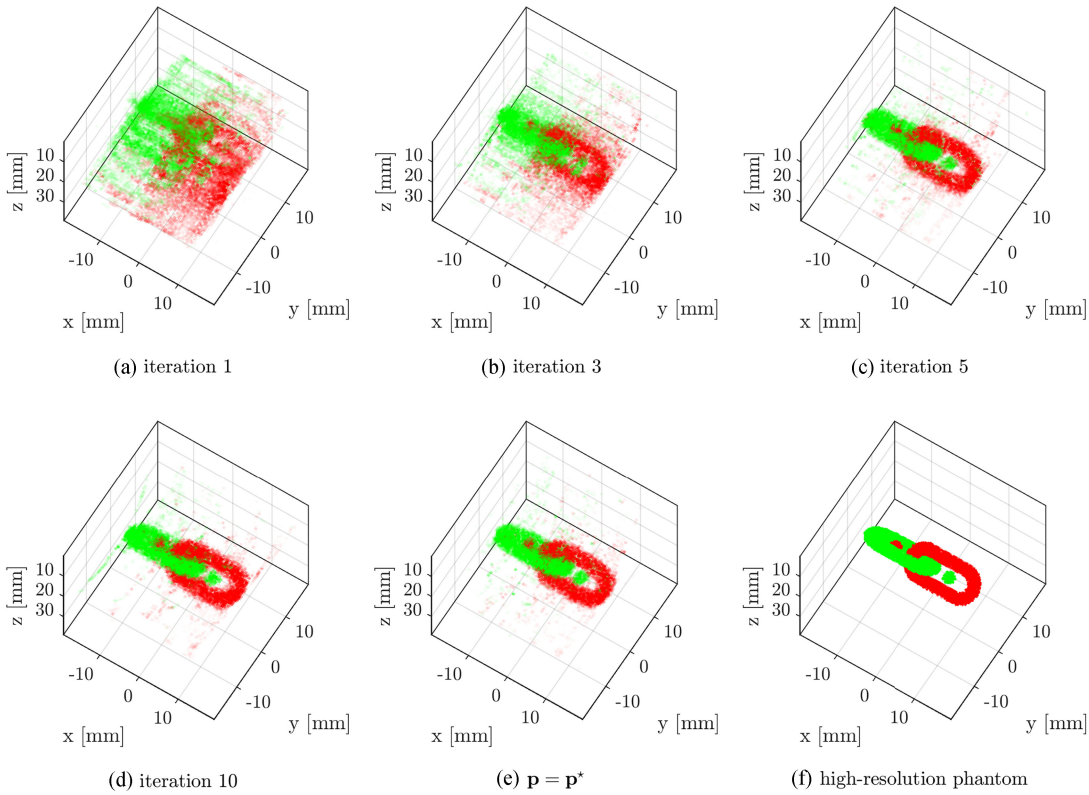

(a) iteration 1 (b) iteration 3 (c) iteration 5

(d) iteration 10 (e) $\mathbf{p} = \mathbf{p}^{\star}$ (f) high-resolution phantom

Fig. 6. 3D reconstruction while solving elevational probe motion using Algorithm 3. The reconstructed volume $\mathbf{x}^{(k)}$ has $64 \times 64 \times 64$ voxels for each chromophore, where k represents the outer iteration count. (a) The $\mathbf{x}^{(1)}$ reconstruction, generated after 1st outer iteration using initial position estimate $\mathbf{p}^{(0)}$. The (b) $\mathbf{x}^{(3)}$ reconstruction, (c) $\mathbf{x}^{(5)}$ reconstruction, and (d) $\mathbf{x}^{(10)}$ reconstruction. (e) Reconstruction with a single outer iteration when probe position $\mathbf{p}$ is initially set to ground truth $\mathbf{p}^{\star}$. (f) The ground truth $\mathbf{x}^{\star}$ used to simulate measured acoustic waves, which has a denser grid geometry of $128 \times 128 \times 128$ voxels. The y-coordinate position error for (a)-(d) is shown in Figure S-3.

in Figure 7. Mathematical optimization was performed using Algorithm 1. The system matrix H was decomposed into F and G as described in equation (24). An outer iteration count of $n_{\max} = 1$ was specified, using elevational velocity of 1.2 mm/s. 40 frames at 757 nm and 1064 nm wavelengths were processed. The acquisition rate was 10 frames per second, corresponding to a swept aperture of 4 mm. The minimization was solved using TFOCS [69] with 400 inner iterations for F and G. Total variation and sparse L1 regularization were used for $\vartheta(\mathbf{x})$. The reconstructed volume used size $(256 \times 256 \times 128) \times 2$, with grid spacing 0.15 mm/voxel, corresponding to dimensions of 38 mm $\times$ 38 mm $\times$ 19 mm, which extends elevationally beyond the 4 mm acquired zone. In addition to reconstruction of individual 757 nm and 1064 nm wavelengths, in Figure 7, statistical color mapping [4], [70] was used to display regions of high and low relative blood oxygen saturation, overlayed on conventional ultrasound. Using the optimization-based technique, the capsular vessels surrounding the lesion reconstruct with significantly reduced artifact and higher contrast compared to the backprojection-based approach. The lesion corresponds to the $\sim$1 cm diameter dark region centered in the grayscale ultrasound map (as seen in Figure 7a, Figure 7d and Figure 8). A 3D isocontour plot of the reconstructed chromophores is shown in Figure 8.

D. Reconstruction Using Biologically-Equivalent Phantom

Using the proposed techniques, reconstruction was performed on a biologically-equivalent phantom [4] containing vessels filled with oxygenated and deoxygenated blood. Acoustic measurements were processed with mathematical optimization using Algorithm 1, where H is decomposed into F and G using equation (24). This was compared with a previous approach [4] involving 2D backprojection. The contrast-to-background ratio (CBR) was evaluated as function of depth for 757 nm and 1064 nm optical wavelengths, as shown in Figure 9. In the near- and mid-field, CBR improved by a factor of $\sim$20 for 3D mathematical optimization compared to 2D backprojection. The maximum penetration depth was defined by CBR reaching a threshold of 1.5, which occurred at $\sim$43 mm for both methods, at which point the optimization based method filtered out deep vessels that faded into the background. Experimental details and additional results are presented in the Supplemental Materials (Figures S-4 to S-8).

E. Varying of Frame Count and Transducer Geometry

We examined the ability to suppress out-of-plane acoustic interference using the digital phantom shown in Figure 10. Two spherical absorbers are arranged such that one sphere

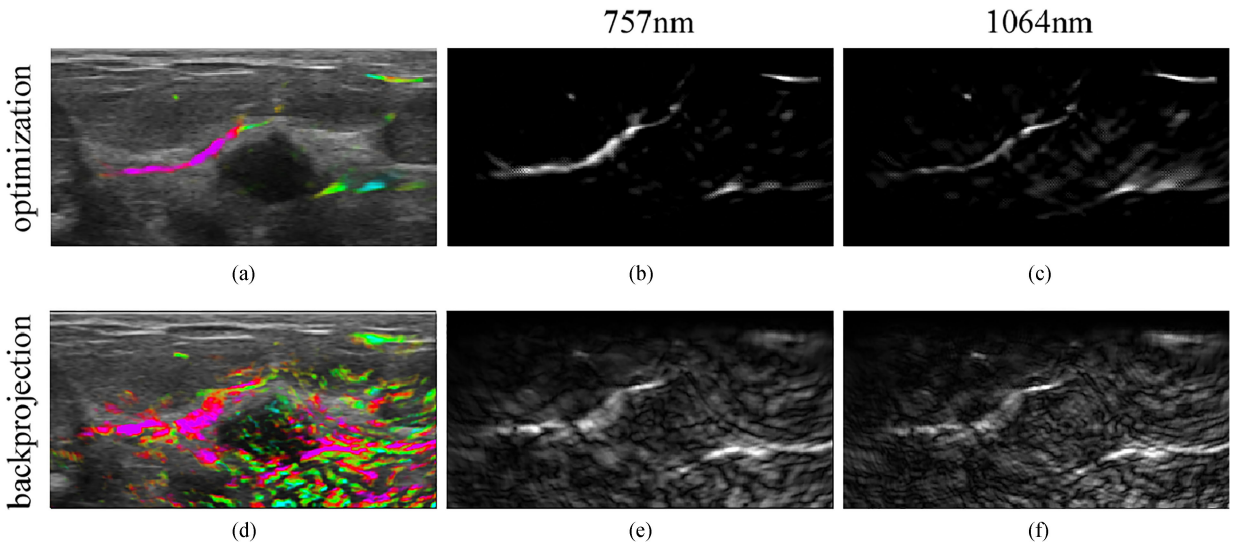

Fig. 7. Opto-acoustic images of a benign breast lesion. Images are generated from OA measurements obtained during a clinical feasibility study [3]. Reconstruction involved (a)–(c) mathematical optimization with Algorithm 1 and (d)–(f) formula-based backprojection. Capsular vessels that surround the lesion are visible using OA. In (a) and (d), colorized OA data is overlayed on conventional grayscale ultrasound to indicate regions of HbO_2 (green) and HHb (red). The 757 nm wavelength for (b) and (e) is absorbed preferentially by HHb. The 1064 nm wavelength for (c) and (f) is absorbed preferentially by HbO_2. Image dimensions are 38 $\times$ 19 mm.

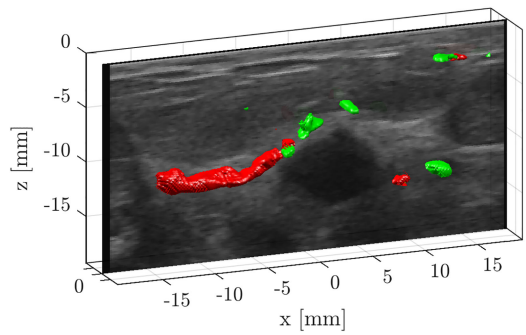

Fig. 8. Reconstructed 3D volume of benign lesion using the proposed technique. Oxygenated (green) and deoxygenated (red) hemoglobin are displayed using isocontours of the 3D chromophore difference map $\mathbf{x}_{\mathrm{HHb}} - \mathbf{x}_{\mathrm{HbO_2}}$. A 2D grayscale ultrasound image is shown in the plane $y = 0$ to identify the lesion, a central dark region from z =10 mm to 15 mm depth.

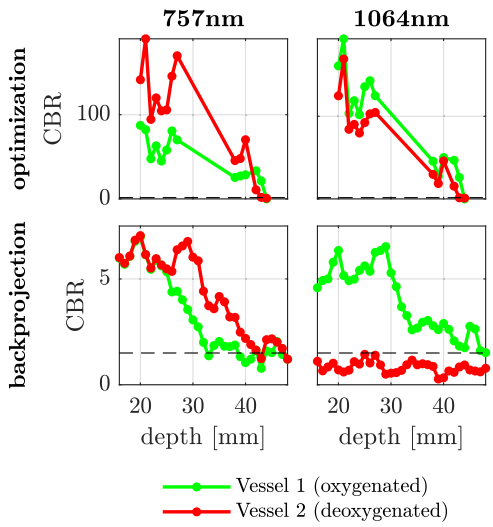

Fig. 9. Contrast-to-background ratio (CBR) of oxygenated and deoxygenated vessels in biologically-equivalent phantom. Results for the proposed optimization-based technique (top row) and backprojection-based technique (bottom row) are plotted for optical wavelengths of 757 nm (left column) and 1064 nm (right column). The dotted line (CBR = 1.5) indicates the threshold to determine maximum penetration depth.

causes interference (for a 2D imaging slice) when the probe is positioned over the other. Simulated datasets were generated with frame counts of 1, 3, and 15 frames, using two different elevational transducer widths: 0 mm (ideal) and 4 mm (wide). For the datasets with multiple frames, interframe spacings of 10 mm and 1.4 mm were used over a swept aperture of 20 mm. Next, 3D volumes were reconstructed from each dataset using a system matrix that modeled a matching or non-matching transducer width (3 cases). Two methods for reconstruction were compared: i) performing minimization using Equation (27); and, ii) performing backprojection based on the operator adjoint of Equation (15). Peak-signal-to-noise ratio (PSNR) was analyzed. The results are summarized in Table II. As shown, the PSNR improved with mathematical optimization, with higher frame counts, and with matching transducer geometries. Additional details and results are presented in the Supplemental Materials (Figures S-9 to S-15).

VI. Discussion

In Section V-A, we demonstrated multi-wavelength reconstruction using frames acquired as the probe followed a curved trajectory. This illustrates that the model described in Section III was able to reconstruct a phantom consisting of multiple chromophores.

Due to the trajectory's radius of curvature, there was different effective spacing between frames at one side of phantom compared to the other, which can be seen in Figure 4. Visually,

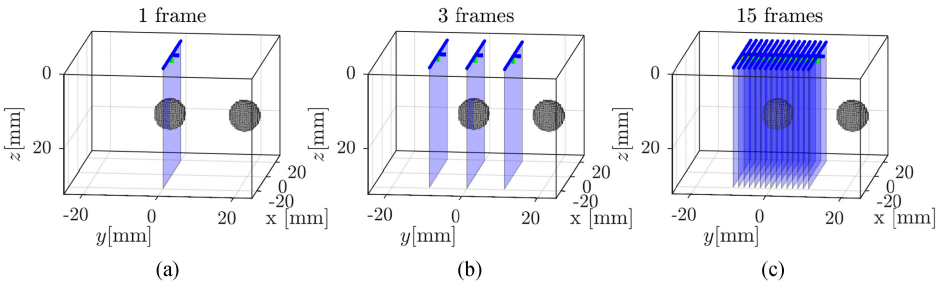

Fig. 10. 3D volume with spherical absorbers. A linear array (blue line) acquires (a) 1 frame, (b) 3 frames, and (c) 15 frames. The imaging plane (light blue) is shown for each frame.

TABLE II
SUMMARY OF PSNR FOR 3D RECONSTRUCTED VOLUMES

Case	Figure	Frames	PSNR Optimization	PSNR Backprojection
1. ideal/ideal	S-11	1	24.7 dB	24.2 dB
		3	27.9 dB	25.7 dB
		15	30.8 dB	25.9 dB
2. wide/ideal	S-12	1	19.9 dB	23.9 dB
		3	18.7 dB	25.2 dB
		15	19.8 dB	25.0 dB
3. wide/wide	S-13	1	25.8 dB	24.8 dB
		3	27.2 dB	25.4 dB
		15	30.3 dB	24.9 dB

this did not lead to degradation in the reconstruction shown in Figure 5. However, if the spacing between frames (or curvature) were significantly increased, this would likely lead to degradation of the reconstruction, as side-lobe and grating-lobe artifact may result. Further examination of this phenomenon is the subject of future work.

In general, the optimal grid size can be influenced by the probe velocity (i.e. the spacing between frames). Performance may depend on the spatial frequency content of the image being reconstructed, with lower resolution images permitting a greater spacing. In this work, grid size was specified independent of probe motion, with consideration for spacing between linear array elements. The regularization parameters in equation (28), which control image sparsity and smoothness, were empirically tuned for performance in each experiment presented in Section V. Optimal values depend on noise level, frame spacing and other a-priori assumptions about the image content. While adjustment of these parameters may impact PSNR, a full analysis of how reconstruction error scales with the regularization parameters is beyond the scope of this paper. In compressive sensing, mathematical optimization is used to overcome theoretical limits of the number of sampled measurements [71]. Analyzing how this applies to frame spacing is a subject for future work.

When using only one frame of linear array data, 3D reconstruction is underdetermined due to rotational symmetry about the array's axis. While sufficient for 2D imaging, this is why our approach reconstructs 3D images using multiple frames. Interestingly, analysis conducted in Section C of the Supplemental Materials suggests that modeling transducer directivity can improve localization of out-of-plane sources in the single-frame case, which is a subject for future work.

While our approach focuses on linear arrays, the acoustic response matrix H_0 in equation (14) can easily be adapted to describe any probe geometry (e.g. 2D or concave arrays), although the computational simplifications of Section III-C may not apply. Compared to linear arrays, matrix arrays can provide more accurate reconstruction by localizing the arrival directions from out-of-plane sources. With a matrix array, a 3D volume of vascular patterns can be accurately reconstructed from a single frame acquisition, which is ideal for performing correlation-based motion tracking [41]. As well, concave arrays help reduce geometric distortion, preventing suppression of directional waves by orienting the transducer elements normal to the array's curvature.

Deformation and internal tissue motion between frames can impact performance of the proposed approach. An extension to include first-order tissue deformation can be implemented by permitting non-rigid affine transformations. This would involve defining configuration $\mathbf{p}_j$ with the vectorized elements of $A_j \in \mathbb{R}^{3\times3}$, as modeled with system matrix $H_{\mathbf{p}}$, and solved using equation (33). In this case, separability of $H_{\mathbf{p}}$ is not maintained, but would be approximate for small deformations.

In Section V-D, we analyzed penetration depth by measuring CNR using a biologically equivalent phantom. This is largely independent of modeled light distribution Φ because the contrast depends on actual light reaching a target relative to its local background (assuming negligible fluence variation in small regions). Nevertheless, suppression of background artifact is dependent on the selection of regularization parameters. While improper modeling of light and other parameters may reduce quantitative accuracy of chromophore measurements, characterization of this was beyond the scope of our work. Instead, we displayed molecular contrast using a non-quantitative statistical color mapping approach [4] that relies on relative image intensities rather than quantitative measurements.

Several related motion detection and reconstruction approaches have been studied in ultrasound imaging, where motion is determined by sensors, or by computing correlations of ultrasonic speckle [32]–[40]. For several reasons, including differences in elevational resolution and speckle characteristics, these ultrasound-based approaches are not generally applicable to OA. Nevertheless, in OA, correlation-based approaches can readily track lateral (in-plane) motion along the linear array's axis; however, elevational (out-of-plane) motion, perpendicular

to the array, is more difficult to estimate, which is an advantage of our approach. Since image reconstruction and motion tracking are combined, in our approach variables representing probe motion are solved simultaneously with variables that represent image voxels. In this formulation, we find that out-of-plane OA sources can actually benefit elevational motion estimation by acting as targets to "lock onto". The results of Section V-B demonstrate how our approach can solve elevational motion in multi-frame acquistion, without using external sensors. Results of Section V-C suggest the proposed technique could potentially lead to significant image quality improvements in systems using linear-array OA probes.

The implementation in Section V-B used constant elevational probe velocity to demonstrate our approach. While our method in Section IV-C supports general probe motion, confinement to a constant velocity is faster computationally and the solution converges robustly by filtering the trajectory, approximating it for small motion segments. Future work involves demonstrating the solution for a general trajectory, and performing continual tracking using segments of piecewise constant velocity.

Additional constraints $\mathcal{C}$ to improve motion tracking are also possible. For example, the trajectory $\mathbf{p}$ can be constrained to ensure probe motion is smooth and continuous, which is achievable using the constraint $\|Q(\mathbf{p}+\Delta\mathbf{p})\| \leq \sigma$, where matrix Q computes finite-difference velocity (or acceleration) of frames in $\mathbf{p}$, and σ is a constant. Techniques involving ℓ_1 trend fitting [72] can also be used to implement smoothness of the trajectory. Moreover, for sequential convex optimization, constraining motion to a region where the problem is likely to be convex [42]–[45], [59], [60] can be achieved by limiting $\mathbf{p}^{(k)} + \Delta\mathbf{p}^{(k+1)}$ to a range of valid values using box constraints. Additionally, constraints may specify boundary conditions for motion at the initial or final frames of $\mathbf{p}$ using first or second motion derivatives. To perform "sensor-fusion," constraints can be used to bind the probe trajectory with external sensor measurements. For example, if position sensors measure a probe configuration $\tilde{\mathbf{p}}$, which may have limited accuracy, then minimizing equation (33) with the constraint $\|\mathbf{p}-\tilde{\mathbf{p}}\| \leq \sigma$ will limit deviation from sensor measurements, thereby combining input from motion sensors into our technique. Future work involves comparing computed trajectories to that obtained by sensors.

VII. Conclusion

This article presented an approach to simultaneously reconstruct 3D images and solve motion for an OA probe using sequential convex optimization. The model developed in Section III was used to implement the 3D reconstruction algorithms described in Section IV. We demonstrated that 3D volumes with multiple chromophores could be reconstructed from 2D OA probe measurements obtained at multiple optical wavelengths. The ability to determine elevational probe velocity was demonstrated in Section V-B using a 3D digital phantom. We demonstrated improvement in CBR and PSNR by analyzing reconstruction with phantoms (Supplemental Materials). Reconstruction of data from a clinical study (Section V-C) suggested the proposed technique potentially enables significant image quality improvements in clinical settings. Future work includes additional tests involving more complex motion trajectories; determining the effect of different probe motion on reconstructed image quality to further characterize the algorithm; and, implementation for a real-time imaging system.

Appendix

The accelerated proximal gradient method [48], [49], [53], [55] solves a convex optimization problem of the form

$$\underset{\mathbf{x}}{\text{minimize}} \quad f(\mathbf{x}) + g(\mathbf{x}) \tag{A.1}$$

where g is a smooth convex function (e.g. the ℓ_2 norm), and f is a non-smooth convex function (e.g. the ℓ_1 norm). This can implement an image reconstruction problem similar to equation (9). The solution of (A.1) is iteratively obtained as

$$\begin{aligned} \mathbf{x}^{k+1} &:= \text{prox}_{\rho f}\left(\mathbf{w}^k - \rho\nabla g(\mathbf{w}^k)\right) \\ \mathbf{w}^{k+1} &:= \mathbf{x}^{k+1} + \beta_k(\mathbf{x}^{k+1} - \mathbf{x}^k) \end{aligned} \tag{A.2}$$

where ρ is a scaling parameter, $\beta_k = \frac{k}{k+3}$, and k is the iteration count. The initial values $\mathbf{x}^0$ and $\mathbf{w}^0$ are set to zero. Since g is smooth, its gradient ∇g can be computed analytically. For the non-smooth function, the *proximal operator* of f is defined as

$$\text{prox}_{\tau f}(\mathbf{x}) = \underset{\mathbf{u}}{\text{argmin}}\left(f(\mathbf{u}) + \frac{1}{2\tau}\|\mathbf{u}-\mathbf{x}\|_2^2\right) \tag{A.3}$$

where τ is a scaling constant. Many non-smooth functions have a proximal operator prox_f that is efficient to compute. However, when a function f is composed with linear operator G, the resulting function $f \circ G$ does not necessarily have a similarly efficient proximal operator.

To deal with such a situation, the ADMM algorithm [52], [55] solves a convex optimization problem of the form

$$\begin{aligned} &\underset{\mathbf{x},\mathbf{z}}{\text{minimize}} \quad g(\mathbf{z}) + \vartheta(\mathbf{x}) \\ &\text{subject to} \quad \mathbf{z} = G\mathbf{x} \end{aligned} \tag{A.4}$$

Here, the variables $\mathbf{x}$ and $\mathbf{z}$ are both minimized. The solution to (A.4) is achieved by iteratively computing

$$\begin{aligned} \mathbf{z}^{k+1} &:= \underset{\mathbf{z}}{\text{argmin}}\left(g(\mathbf{z}) + \frac{\rho}{2}\|\mathbf{z} - G\mathbf{x}^k - \mathbf{u}^k\|_2^2\right) \\ \mathbf{x}^{k+1} &:= \underset{\mathbf{x}}{\text{argmin}}\left(\vartheta(\mathbf{x}) + \frac{\rho}{2}\|G\mathbf{x} - \mathbf{z}^{k+1} + \mathbf{u}^k\|_2^2\right) \\ \mathbf{u}^{k+1} &:= \mathbf{u}^k + G\mathbf{x}^{k+1} - \mathbf{z}^{k+1} \end{aligned} \tag{A.5}$$

where $\mathbf{u}$ is a dual-update variable, and ρ is a scaling parameter. In Section IV, equation (A.5) is used to derive an algorithm for 3D reconstruction.

The TFOCS solver [57], [69] can handle a convex optimization problem in block composite form (BCF), represented as

$$\underset{\mathbf{v}}{\text{minimize}} \quad \xi_0(\mathbf{v}) + \sum_{i=1}^{m} \xi_i(L_i\mathbf{v} - \mathbf{c}_i) \tag{A.6}$$

where

$$L = \begin{bmatrix} L_1 \\ \vdots \\ L_m \end{bmatrix}, \qquad \mathbf{c} = \begin{bmatrix} \mathbf{c}_1 \\ \vdots \\ \mathbf{c}_m \end{bmatrix}$$

Here, L is a block matrix containing m linear operator matrices L_i, and $\mathbf{c}_i$ is an offset vector. The smooth function ξ_0 is applied

to the composite vector $\mathbf{v}$, and the functions ξ_i, $i = 1 \dots m$ are applied to the domain $L_i\mathbf{v} - \mathbf{c}_i$. For convenience, in (A.6) the summation $\sum_{i=1}^{m} \xi_i(L_i\mathbf{v} - \mathbf{c}_i)$ can be written $\boldsymbol{\xi}(L\mathbf{v} - \mathbf{c})$, where $\boldsymbol{\xi} = [\xi_1, \dots, \xi_m]$ is a function map. The TFOCS solver, rather than solving equation (A.6) directly, minimizes a dual optimization problem of the form

$$\underset{\mathbf{u}}{\text{minimize}} \quad \xi_0^* \left(\sum_{i=1}^{m} L_i^T \mathbf{u}_i \right) + \sum_{i=1}^{m} \xi_i^*(-\mathbf{u}_i + \mathbf{c}_i) \tag{A.7}$$

where $\xi_0^*(\mathbf{v})$ is the dual conjugate of $\xi_0(\mathbf{v})$ and $\xi_i^*(\mathbf{u})$ is the dual conjugate of $\xi_i(\mathbf{v})$ [57], [69]. This computation is more efficient because the linear operator matrices L_i are moved from the non-smooth functions ξ_i in (A.6) to the smooth function ξ_0^* in (A.7). In this case, solving (A.7) with (A.2) requires the smooth-function gradient $\nabla\xi_0^* = \text{prox}_{\xi_0}$ and the dual-proximal operator $\text{prox}_{\boldsymbol{\xi}^*}$, which can be obtained from $\text{prox}_{\boldsymbol{\xi}}$ using a mathematical identity [48], [57]. Accordingly, the solution of (A.7) is computed iteratively as

$$\begin{aligned} \mathbf{v}^{k+1} &:= \text{prox}_{\tau\xi_0}(\mathbf{v}^{k-\alpha_k} + \tau L^T \mathbf{w}^k) \\ \mathbf{u}^{k+1} &:= \mathbf{c} - \text{prox}_{\sigma\boldsymbol{\xi}^*}(\mathbf{c} - \mathbf{w}^k + \sigma L \mathbf{v}^{k+1}) \\ \mathbf{w}^{k+1} &:= \mathbf{u}^{k+1} + \beta_k(\mathbf{u}^{k+1} - \mathbf{u}^k) \end{aligned} \tag{A.8}$$

where $\beta_k = \frac{k}{k+3}$, $\alpha_k = k - a\lfloor \frac{k}{a} \rfloor$, with $a \in \mathbb{Z}^+$, and σ and τ are scaling parameters.

ACKNOWLEDGMENT

The authors wish to thank Y. Xu, C. J. Kumaradas, Y. Bismilla, B. A. Clingman, S. C. Miller, T. G. Miller and D. G. Herzog for discussions regarding this manuscript. Datasets for Sections V-C and V-D were provided by Seno Medical Instruments, Inc.

REFERENCES

[1] E. I. Neuschler *et al.*, "A pivotal study of optoacoustic imaging to diagnose benign and malignant breast masses: A new evaluation tool for radiologists," *Radiology*, vol. 287, no. 2, pp. 398–412, 2018.

[2] A. A. Oraevsky, B. Clingman, J. Zalev, A. T. Stavros, W. T. Yang, and J. R. Parikh, "Clinical optoacoustic imaging combined with ultrasound for coregistered functional and anatomical mapping of breast tumors," *Photoacoustics*, vol. 12, pp. 30–45, 2018.

[3] J. Zalev *et al.*, "Opto-acoustic image fusion technology for diagnostic breast imaging in a feasibility study," in *Proc. SPIE Med. Imaging. Int. Soc. Opt. Photon.*, 2015, pp. 941909–941909.

[4] J. Zalev *et al.*, "Opto-acoustic imaging of relative blood oxygen saturation and total hemoglobin for breast cancer diagnosis," *J. Biomed. Opt.*, vol. 24, no. 12, 2019, Art. no. 121915.

[5] N. Nyayapathi and J. Xia, "Photoacoustic imaging of breast cancer: A mini review of system design and image features," *J. Biomed. Opt.*, vol. 24, no. 12, 2019, Art. no. 121911.

[6] S. Manohar and M. Dantuma, "Current and future trends in photoacoustic breast imaging," *Photoacoustics*, vol. 16, 2019, Art. no. 100134, doi: 10.1016/j.pacs.2019.04.004.

[7] S. Zackrisson, S. Van De Ven, and S. S. Gambhir, "Light in and sound out: Emerging translational strategies for photoacoustic imaging," *Cancer Res.*, vol. 74, no. 4, pp. 979–1004, 2014.

[8] P. K. Upputuri and M. Pramanik, "Recent advances toward preclinical and clinical translation of photoacoustic tomography: A review," *J. Biomed. Opt.*, vol. 22, no. 4, 2016, Art. no. 041006.

[9] K. S. Valluru and J. K. Willmann, "Clinical photoacoustic imaging of cancer," *Ultrasonography*, vol. 35, no. 4, pp. 267–280, 2016.

[10] K. S. Valluru, K. E. Wilson, and J. K. Willmann, "Photoacoustic imaging in oncology: Translational preclinical and early clinical experience," *Radiology*, vol. 280, no. 2, pp. 332–349, 2016.

[11] A. P. Rao, N. Bokde, and S. Sinha, "Photoacoustic imaging for management of breast cancer: A literature review and future perspectives," *Applied Sci.*, vol. 10, no. 3, pp. 2076–3417, 2020.

[12] R. K. Jain, "Normalizing tumor microenvironment to treat cancer: Bench to bedside to biomarkers," *J. Clin. Oncol.*, vol. 31, no. 17, pp. 2205–2218, 2013.

[13] P. Carmeliet and R. K. Jain, "Angiogenesis in cancer and other diseases," *Nature*, vol. 407, no. 6801, pp. 249–257, 2020.

[14] G. Bergers and L. E. Benjamin, "Tumorigenesis and the angiogenic switch.," *Nat. Rev. Cancer*, vol. 3, no. 6, P. 401–410, 2003.

[15] M. Papetti and I. M. Herman, "Mechanisms of normal and tumor-derived angiogenesis," *Amer. J. Physiol.-Cell Physiol.*, vol. 282, no. 5, pp. C947–C970, 2002.

[16] R. K. Jain, "Taming vessels to treat cancer," *Sci. Amer.*, vol. 298, no. 1, pp. 56–63, 2008.

[17] M. Xu and L. V. Wang, "Universal back-projection algorithm for photoacoustic computed tomography," *Phys. Rev.*, vol. 71, no. 1, 2005, Art. no. 016706.

[18] A. A. Oraevsky, "Optoacoustic tomography: From fundamentals to diagnostic imaging of breast cancer," in *Biomed. Photon. Handbook*. CRC Press, 2014, pp. 738–781.

[19] M. A. Anastasio, J. Zhang, D. Modgil, and P. J. La Rivière, "Application of inverse source concepts to photoacoustic tomography," *Inverse Problems*, vol. 23, no. 6, pp. S21–S35, 2007.

[20] P. Kuchment and L. Kunyansky, "Mathematics of photoacoustic and thermoacoustic tomography," in *Handbook Math. Methods Imag.*, Springer, 2011, pp. 817–865.

[21] A. Rosenthal, V. Ntziachristos, and D. Razansky, "Acoustic inversion in optoacoustic tomography: A review," *Current Med. Imag.*, vol. 9, no. 4, pp. 318–336, 2013.

[22] K. Wang, R. Su, A. A. Oraevsky, and M. A. Anastasio, "Investigation of iterative image reconstruction in three-dimensional optoacoustic tomography," *Physics Med. Biol.*, vol. 57, no. 17, 2012, Art. no. 5399.

[23] K. Wang, S. A. Ermilov, R. Su, H.-P. Brecht, A. A. Oraevsky, and M. A. Anastasio, "An imaging model incorporating ultrasonic transducer properties for three-dimensional optoacoustic tomography," *IEEE Trans. Med. Imag.*, vol. 30, no. 2, pp. 203–214, Feb. 2011.

[24] J. Provost and F. Lesage, "The application of compressed sensing for photo-acoustic tomography," *IEEE Trans. Med. Imag.*, vol. 28, no. 4, pp. 585–594, Apr. 2009.

[25] K. Wang, C. Huang, Y.-J. Kao, C.-Y. Chou, A. A. Oraevsky, and M. A. Anastasio, "Accelerating image reconstruction in three-dimensional optoacoustic tomography on graphics processing units," *Med. Phys.*, vol. 40, no. 2, 2013, Art. no. 023301, doi: 10.1118/1.4774361.

[26] L. Ding, X. L. Deán-Ben, N. C. Burton, R. W. Sobol, V. Ntziachristos, and D. Razansky, "Constrained inversion and spectral unmixing in multispectral optoacoustic tomography," *IEEE Trans. Med. Imag.*, vol. 36, no. 8, pp. 1676–1685, Aug. 2017.

[27] J. Zalev and M. C. Kolios, "Image reconstruction combined with interference removal using a mixed-domain proximal operator," *IEEE Signal Process. Lett.*, vol. 25, no. 12, pp. 1840–1844, Dec. 2018.

[28] J. Zalev and M. C. Kolios,"Fast three-dimensional opto-acoustic simulation for linear array with rectangular elements," *IEEE Trans. Ultrason., Ferroelect. Freq. Control*, vol. 68, no. 5, pp. 1885–1906, May 2021.

[29] H. Dirks, "Variational Methods for Joint Motion Estimation and Image Reconstruction," PhD thesis. University of Münster, Germany, 2015.

[30] F. Lucka *et al.*, "Enhancing compressed sensing 4D photoacoustic tomography by simultaneous motion estimation," *SIAM J. Imag. Sci.*, vol. 11, no. 4, pp. 2224–2253, 2018.

[31] H. J. Kang, M. A. L. Bell, X. Guo, and E. M. Boctor, "Spatial angular compounding of photoacoustic images," *IEEE Trans. Med. Imag.*, vol. 35, no. 8, pp. 1845–1855, Aug. 2016.

[32] C. Laporte and T. Arbel, "Learning to estimate out-of-plane motion in ultrasound imagery of real tissue," *Med. Imag. Anal.*, vol. 15, no. 2, pp. 202–213, 2011.

[33] N. Afsham, A. Rasoulian, M. Najafi, P. Abolmaesumi, and R. Rohling, "Nonlocal means filter-based speckle tracking," *IEEE Trans. Ultrason. Ferroelect., Freq. Control*, vol. 62, no. 8, pp. 1501–1515, Aug. 2015.

[34] P. Coupé, P. Hellier, N. Azzabou, and C. Barillot, "3D freehand ultrasound reconstruction based on probe trajectory," in *Proc. Int. Conf. Med. Image Comput. Comput.- Assist. Interv.*, Springer, 2005, pp. 597–604.

[35] O. V. Solberg, F. Lindseth, H. Torp, R. E. Blake, and T. A. N. Hernes, "Freehand 3D ultrasound reconstruction algorithms—A review," *Ultrasound Med. Biol.*, vol. 33, no. 7, pp. 991–1009, 2007.

[36] H. Yu, M. S. Pattichis, C. Agurto, and M. B. Goens, "A 3D freehand ultrasound system for multi-view reconstructions from sparse 2D scanning planes," *Biomed. Eng. Online*, vol. 10, no. 1, pp. 1-22, 2011.
[37] R. Rohling, A. Gee, and L. Berman, "A comparison of freehand three-dimensional ultrasound reconstruction techniques," *Med. Image Anal.*, vol. 3, no. 4, pp. 339–359, 1999.
[38] A. Lang, P. Mousavi, S. Gill, G. Fichtinger, and P. Abolmaesumi, "Multi-modal registration of speckle-tracked freehand 3D ultrasound to CT in the lumbar spine," *Med. Image Anal.*, vol. 16, no. 3, pp. 675–686, 2012.
[39] A. Fenster, D. B. Downey, and H. N. Cardinal, "Three-dimensional ultrasound imaging," *Physics Med. Biol.*, vol. 46, no. 5, pp. R67–R99, 2001.
[40] J. Ng, R. Prager, N. Kingsbury, G. Treece, and A. Gee, "Modeling ultrasound imaging as a linear, shift-variant system," *IEEE Trans. Ultrason., Ferroelect., Freq. Control*, vol. 53, no. 3, pp. 549–563, Mar. 2006.
[41] N. Knauer, X. L. Deán-Ben, and D. Razansky, "Spatial compounding of volumetric data enables freehand optoacoustic angiography of large-scale vascular networks," *IEEE Trans. Med. Imag.*, vol. 39, no. 4, pp. 1160–1169, Apr. 2020.
[42] K. Song and M. Horowitz, "Tomographic reconstruction and alignment using matrix norm minimization," *J. Sel. Top. Signal Process.*, vol. 10, no. 1, pp. 47–60, 2016.
[43] A. Y. Yang, Z. Zhou, A. G. Balasubramanian, S. S. Sastry, and Y. Ma, "Fast ℓ_1-minimization algorithms for robust face recognition," *IEEE Trans. Image Process.,* vol. 22, no. 8, pp. 3234–3246, Aug. 2013.
[44] A. Wagner, J. Wright, A. Ganesh, Z. Zhou, H. Mobahi, and Y. Ma, "Toward a practical face recognition system: Robust alignment and illumination by sparse representation," *IEEE Trans. Pattern Anal. Mach. Intell.*, vol. 34, no. 2, pp. 372–386, Feb. 2012.
[45] Y. Peng, A. Ganesh, J. Wright, W. Xu, and Y. Ma, "RASL: Robust alignment by sparse and low-rank decomposition for linearly correlated images," *IEEE Trans. Pattern Ana. Mach. Intell.*, vol. 34, no. 11, pp. 2233–2246, Nov. 2012.
[46] L. Condat, "A primal-dual splitting method for convex optimization involving lipschitzian, proximable and linear composite terms," *J. Optim. Theory Appl.*, vol. 158, no. 2, pp. 460–479, 2013.
[47] N. Komodakis and J.-C. Pesquet, "Playing with duality: An overview of recent primal? dual approaches for solving large-scale optimization problems," *IEEE Signal Process. Mag.*, vol. 32, no. 6, pp. 31–54, Nov. 2015.
[48] P. L. Combettes and J. Pesquet, "Proximal splitting methods in signal processing," in *Proc. Fixed-Point Algorithms Inverse Problems Sci. Eng.,* Springer, 2011, pp. 185–212.
[49] A. Beck and M. Teboulle, "Fast gradient-based algorithms for constrained total variation image denoising and deblurring problems," *IEEE Trans. Image Process.*, vol. 18, no. 11, pp. 2419–2434, Nov. 2009.
[50] M. T. McCann *et al.*, "Biomedical image reconstruction: from the foundations to deep neural networks," *Found. Trends Signal Process.*, vol. 13, no. 3, pp. 283–359, 2019.
[51] S. Boyd and L. Vandenberghe, *Convex Optimization*. Cambridge, U.K.: Cambridge Univ. Press, 2004.
[52] S. Boyd *et al.*, "Distributed optimization and statistical learning via the alternating direction method of multipliers," *Found. Trends Mach. Learn.*, vol. 3, no. 1, pp. 1–122, 2011.
[53] S. R. Becker, E. J. Candès, and M. C. Grant, "Templates for convex cone problems with applications to sparse signal recovery," *Math. Program. Comput.*, vol. 3, no. 3, pp. 165–218, 2011.
[54] V. Cevher, S. Becker, and M. Schmidt, "Convex optimization for Big Data: Scalable, randomized, and parallel algorithms for Big Data analytics," *IEEE Signal Process. Mag.*, vol. 31, no. 5, pp. 32–43, Sep. 2014.
[55] N. Parikh *et al.*, "Proximal algorithms," *Found. Trends Optim.*, vol. 1, no. 3, pp. 127–239, 2014.
[56] T. Goldstein, M. Li, X. Yuan, E. Esser, and R. Baraniuk, "Adaptive primal-dual hybrid gradient methods for saddle-point problems," 2013. *arXiv:1305.0546.*
[57] A. Y. Aravkin and S. Becker, "Dual smoothing and level set techniques for variational matrix decomposition," 2016. *arXiv:1603.00284.*
[58] M. Zibulevsky and M. Elad, "L1-L2 Optimization in signal and image processing," *IEEE Signal Process. Mag.*, vol. 27, no. 3, pp. 76–88, May 2010.
[59] J. Nocedal and S. J. Wright, "Sequential quadratic programming," in *Proc. Numer. Optim.,* 2006, pp. 529–562.
[60] L. Etman, A. A. Groenwold, and J. Rooda, "First-order sequential convex programming using approximate diagonal QP subproblems," *Struct. Multidisciplinary Optim.*, vol. 45, no. 4, pp. 479–488, 2012.
[61] A. Liemert and A. Kienle, "Analytical approach for solving the radiative transfer equation in two-dimensional layered media," *J. Quantitative Spectrosc. Radiative Transfer*, vol. 113, no. 7, pp. 559–564, 2012.
[62] A. Liemert and A. Kienle, "Light transport in three-dimensional semi-infinite scattering media," *JOSA A*, vol. 29, no. 7, pp. 1475–1481, 2012.
[63] T. J. Farrell, M. S. Patterson, and B. Wilson, "A diffusion theory model of spatially resolved, steady-state diffuse reflectance for the noninvasive determination of tissue optical properties in vivo," *Med. Phys.*, vol. 19, no. 4, pp. 879–888, 1992.
[64] R. J. Zemp, "Phase-function corrected diffusion model for diffuse reflectance of a pencil beam obliquely incident on a semi-infinite turbid medium," *J. Biomed. Opt.*, vol. 18, no. 6, p. 067005, 2013.
[65] A. H. Hielscher, R. E. Alcouffe, and R. L. Barbour, "Comparison of finite-difference transport and diffusion calculations for photon migration in homogeneous and heterogeneous tissues," *Phys. Med. Biol.*, vol. 43, no. 5, pp. 1285–1302, 1998.
[66] L. Wang, S. L. Jacques, and L. Zheng, "MCML-monte carlo modeling of light transport in multi-layered tissues," *Comput. Methods Programs Biomed.*, vol. 47, no. 2, pp. 131–146, 1995.
[67] B. Wilson and G. Adam, "A Monte Carlo model for the absorption and flux distributions of light in tissue," *Med. Phys.*, vol. 10, no. 6, pp. 824–830, 1983.
[68] E. Chouzenoux, M. Legendre, S. Moussaoui, and J. Idier, "Fast constrained least squares spectral unmixing using primal-dual interior-point optimization," *IEEE J. Sel. Top. Appl. Earth Observ. Remote Sens.*, vol. 7, no. 1, pp. 59–69, Jan. 2014.
[69] S. Becker, E. Candes, and M. Grant,"Templates for convex cone problems with applications to sparse signal recovery," *Math. Program. Comput.* vol. 3, no. 3, pp. 165–218, 2012.
[70] J. Zalev and B. Clingman, "Statistical mapping in an optoacoustic imaging system," US Patent 9,330,452, May 3, 2016.
[71] D. L. Donoho, "Compressed sensing," *IEEE Trans. Inf. Theory*, vol. 52, no. 4, pp. 1289–1306, Apr. 2006.
[72] S. Kim, K. Koh, S. Boyd, and D. Gorinevsky, "ℓ_1 Trend filtering," *SIAM Rev.*, vol. 51, no. 2, pp. 339–360, 2009.

Jason Zalev received the bachelor's degree in electrical/computer engineering in 2006, the Master of Science degree in biomedical physics in 2010, and the Ph.D. degree in biomedical physics in 2021, all from Ryerson University, Toronto, Canada. From 2010 to 2020, he developed optoacoustic image reconstruction algorithms and software used in a diagnostic breast imaging device with Seno Medical Instruments, Inc. He has authored more than 7 peer-reviewed journal publications, 10 papers in conference proceedings and holds 27 granted US patents. His research interests include signal processing, convex mathematical optimization algorithms, image reconstruction, and acoustic physics.

Michael C. Kolios (Member, IEEE) is a Professor with the Department of Physics, Ryerson University and an Associate Dean of Research and Graduate Studies with the Faculty of Science. His work focuses on the use of ultrasound and optics in the biomedical sciences. He has authored or coauthored 140 peer-reviewed journal publications, five book chapters, and 190 papers in conference proceedings. He was the recipient of the numerous teaching and research Awards, including the American Institute of Ultrasound in Medicine Joseph H. Holmes Basic Science Pioneer Award, the Canada Research Chair in Biomedical Applications of Ultrasound and the Ontario Premier's Research Excellence Award. He is on the Editorial Board of the *Journals Ultrasound Imaging and Photoacoustics* and is a member of many national and international committees, including the IEEE INTERNATIONAL ULTRASONICS SYMPOSIUM TECHNICAL PROGRAM COMMITTEE. He regularly reviews for various funding agencies and was a Charter Member of the National Institutes of Health (NIH) Biomedical Imaging Technology of a study section and is a member of the College of Reviewers for the Canadian Institutes of Health Research (CIHR).